Author for correspondence:
Tsevi Beatus
e-mail: tsevi.beatus@cornell.edu

THE ROYAL SOCIETY
PUBLISHING

Controlling roll perturbations in fruit flies

Tsevi Beatus[1], John M. Guckenheimer[2] and Itai Cohen[1]

[1]Department of Physics, and [2]Department of Mathematics, Cornell University, Ithaca, NY 14853, USA

Owing to aerodynamic instabilities, stable flapping flight requires ever-present fast corrective actions. Here, we investigate how flies control perturbations along their body roll angle, which is unstable and their most sensitive degree of freedom. We glue a magnet to each fly and apply a short magnetic pulse that rolls it in mid-air. Fast video shows flies correct perturbations up to $100°$ within 30 ± 7 ms by applying a stroke-amplitude asymmetry that is well described by a linear proportional–integral controller. For more aggressive perturbations, we show evidence for nonlinear and hierarchical control mechanisms. Flies respond to roll perturbations within 5 ms, making this correction reflex one of the fastest in the animal kingdom.

1. Introduction

Locomoting organisms evolved mechanisms to control their motion and maintain stability against mechanical disturbances. The control challenge is prominent in small flying insects since their small moment of inertia renders them susceptible even to gentle air currents [1–4]. Moreover, they fly at Reynolds numbers $Re = 10^2$–10^4, in which flows are unsteady [5,6]. Most importantly, recent analytical and numerical analyses, as well as mechanical models, indicate that flapping flight is aerodynamically unstable, on a time scale of a few wing-beats [7–19]. It is, therefore, intriguing how insects overcome such control challenges and manage to fly with impressive stability, manoeuvrability and robustness, outmanoeuvring any man-made flying device.

Among the body Euler angles—yaw, pitch and roll—roll is most sensitive to perturbing torques since the moment of inertia of the insect's long axis is smallest [1,2]. Recent fluid dynamics simulations suggest roll is *unstable* due to an unsteady aerodynamic mechanism, where roll is positively coupled to sideways motion via asymmetry of the leading-edge vortex attached to each wing [14–18]. The coupling is driven by the wings' flapping and causes the roll angle to grow. Such results indicate that when left uncontrolled, flies can lose their body attitude due to roll perturbations within four wing-beats. In these fluid dynamics simulations, the wings were modelled as rigid plates. Controlling roll is also crucial for maintaining direction and altitude. Thus, any basic understanding of insect flight demands quantitative analysis of roll control.

Previous studies used tethered animals to measure changes in wing motion in response to imposed roll rotations [20–25] and visual roll stimuli [24–30]. In such experiments, however, the tethered insect does not control its motion and often exhibits wing kinematics and torques qualitatively different from those in free flight [31,32]. Tethered [33,34] as well as free-flight [35–38] assays have also been used to study how insects control their head motion for gaze stabilization in response to visual and mechanical stimuli. More recently, free-flight experiments used vortices [1–3] and impulsive gusts [4] to perturb insects, highlighting the sensitivity of the roll angle to perturbations. Understanding roll control, however, requires fast and accurate quantitative measurements of wing and body kinematics in response to controlled mid-air perturbation impulses—a methodology recently applied to study yaw control [39]. Crucially, these previous works typically consider only the linear response [30,39–45]. Whether nonlinear mechanisms come into play in natural free flight, where both large and coupled perturbations are common [1] remains unknown.

Here, we perturb a fruit fly (*Drosophila melanogaster*) by gluing a magnet to its back and applying an approximately 5 ms magnetic pulse that rolls it in
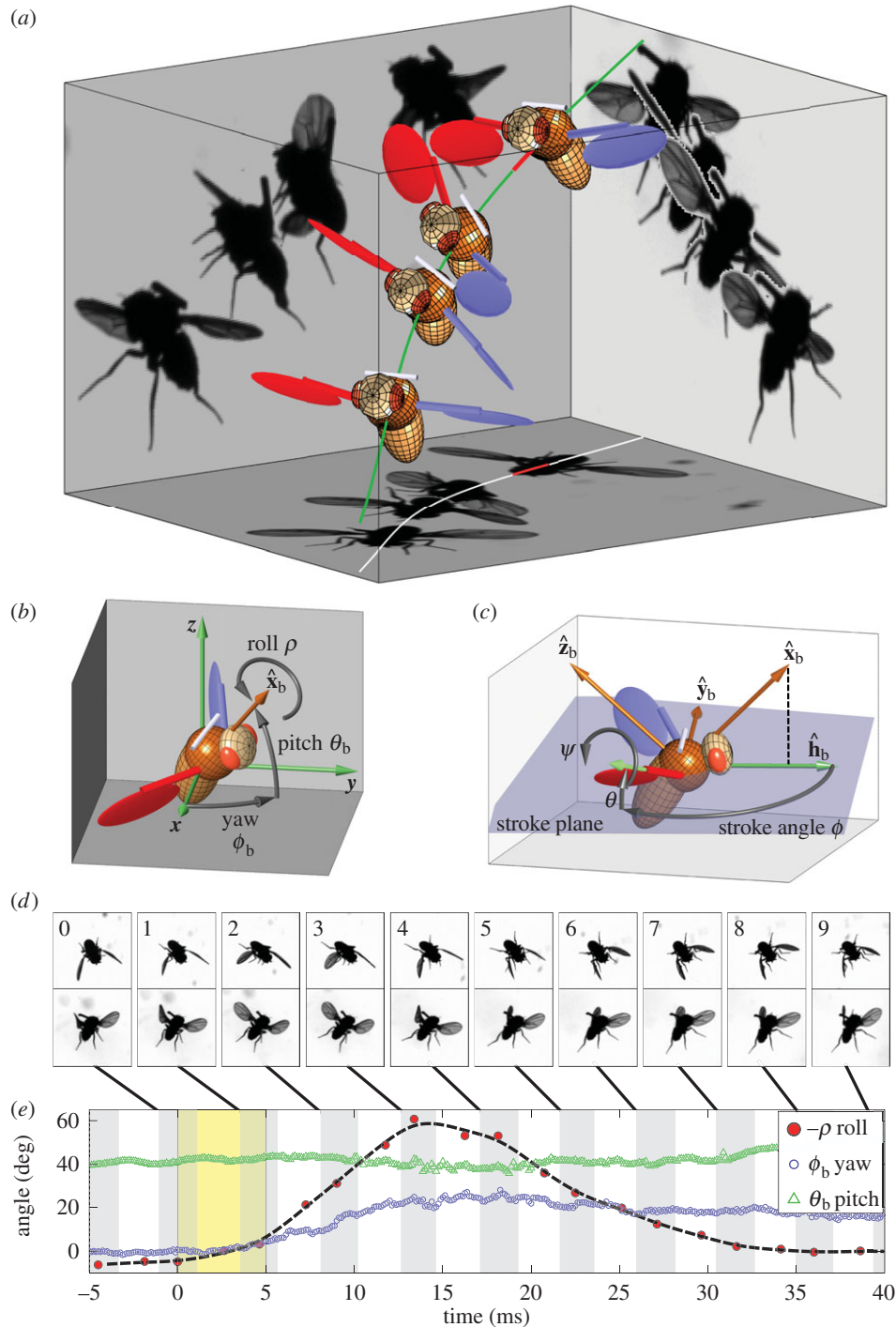
Figure 1. Roll perturbation and correction. (*a*) Images from three orthogonal cameras of a roll correction manoeuvre. The three-dimensional-rendered fly represents the measured kinematics. The perturbation location (red line) is shown on the fly's centre-of-mass trajectory (green). In the second snapshot, the fly is rolled 60° to its left. (*b*) Definition of body Euler angles with respect to the laboratory frame. $\hat{\mathbf{x}}_b$ is the long body axis. (*c*) Definition of the body frame ($\hat{\mathbf{x}}_b$, $\hat{\mathbf{y}}_b$, $\hat{\mathbf{z}}_b$) and wing Euler angles, measured in the body frame with respect to the stroke plane (shaded blue). (*d*) Top and side views of 10 consecutive wing strokes of the manoeuvre, taken when the wings are at their forward-most position. The perturbation wing-beat is numbered 0. (*e*) Body Euler angles versus time. Perturbation was applied between 0 and 5 ms (yellow). White and grey stripes represent forward and back strokes, respectively. Yaw and pitch were sampled at 8000 Hz. Roll was measured manually at the middle of each half-stroke and smoothed by a spline (dashed line). Measurement errors are comparable to the symbol size.

mid-air (figure 1*a*). The perturbation amplitude ranges from roll deflections of 5° to multiple rotations along the roll angle as defined in figure 1*b*. We use high-speed video to film the fly's corrective manoeuvre and measure its wing and body kinematics [46]. We find that for roll perturbations up to 70° flies generate corrective torques by applying a stroke-amplitude asymmetry that is determined by the output of a linear proportional–integral (PI) controller for roll perturbations. The asymmetry starts only one wing-beat (approx. 5 ms) after the perturbation onset, making the roll correction reflex one of the fastest in the animal kingdom [47]. Surprisingly, however, we find that linear control is not sufficient to explain the response for multiple rotations nor the overarching control structure for simultaneously handling yaw, pitch and roll.

2. Material and methods

2.1. Animal preparation

We use common fruit flies (*Drosophila melanogaster*) from an out-bred laboratory stock. After the flies are anaesthetized at a temperature of 0–4°C, we glue a carbon steel pin, 1.5–2 mm long, 0.15 mm in diameter and mass 0.2 mg (Gordon Brush, CA, USA), to the notum, the dorsal surface of the fly's thorax. The pin is glued horizontally, parallel to the line connecting the two wing hinges (figure 1). The pin did not interfere with the motion of the wings. The pin added approximately 20% to the fly's mass, less than the natural fluctuations in its body mass. In addition, the change in the body centre of mass position due to the pin was small, about 3.5% of the body length.

To demonstrate the effect of the pin on the fly's inertia tensor, we estimated the pin inertia and added it to the body-only inertia tensor, I_{body}, calculated in [48]:

$$I_{body} = \begin{pmatrix} I_{xx} & 0 & 0 \\ 0 & I_{yy} & 0 \\ 0 & 0 & I_{zz} \end{pmatrix} = \begin{pmatrix} 1.1 & 0 & 0 \\ 0 & 5 & 0 \\ 0 & 0 & 5 \end{pmatrix} \times 10^{-13} \text{ kg m}^2 \quad (2.1)$$

and

$$I_{body+pin} = \begin{pmatrix} 2.9 & 0 & -0.3 \\ 0 & 6.3 & 0 \\ -0.3 & 0 & 5.7 \end{pmatrix} \times 10^{-13} \text{ kg m}^2. \quad (2.2)$$

The $\hat{x}_b$, $\hat{y}_b$ and $\hat{z}_b$ body axes are defined in figure 1c, such that $\hat{x}_b$ is the roll axis. Note that the moment of inertia tensor is defined in the body frame of reference, such that I_{xx} is the moment of inertia along the $\hat{x}_b$ axis, I_{yy} is the moment of inertia along the $\hat{y}_b$ axis and I_{zz} is the moment of inertia along the $\hat{z}_b$ axis. The inertia tensor of the untreated fly is diagonal since it is well approximated by an ellipsoid. The pin roughly triples the inertia along roll, which means that naturally, without the pin, the fly is three times more susceptible to roll perturbations than in our experiments and is also expected to be more manoeuvrable. Thus, for a given roll perturbation, the recovery times measured in our experiments set an upper bound to the recovery time of naturally occurring flies. The moments of inertia along $\hat{y}_b$ and $\hat{z}_b$ increase by 20%, which is comparable to the increase in mass. The pin's contribution to the off-diagonal terms of the inertia tensor is negligible. Thus, while the pin does change the moment of inertia, it introduces no significant coupling between the rotation axes and roll remains the most sensitive degree of freedom.

2.2. Mid-air perturbations and videography

In each experiment, approximately 15 prepared flies were released in a transparent cubic chamber of side length 13 cm, equipped with two Helmholtz coils that are used to generate a vertical magnetic field (inner diameter 10 cm, outer diameter 12 cm, copper wire diameter 0.8 mm and 240 turns) [39,46]. Three synchronized fast cameras (Phantom v. 7.1, Vision Research) were focused on a cubic filming volume at the centre of the chamber. The side length of the filming volume was either 2.2 or 4.3 cm, such that it was far enough from the chamber boundaries to avoid their effect, for example, owing to take-off and landing manoeuvres. One camera was directed downwards and the other two were directed horizontally, such that cameras are all orthogonal to each other. The cameras operated at 8000 frames s^{-1} and 512×512 pixel resolution. The cameras were back-lit by a red light-emitting diode (Diamond Dragon, Osram Opto Semiconductors) with characteristic wavelength of 625 ± 10 nm (peak $\pm$ spectrum width at 50% intensity). Fruit flies are marginally sensitive to light in this wavelength range [49].

Recording was initiated by an optical trigger consisting of two expanded laser beams (wavelength 633 nm) crossing in the middle of the filming volume and two corresponding photo-diode detectors. When a fly entered the filming volume, the reduction in the laser beam intensity was detected by a custom built circuit that triggered the cameras as well as a 5 ms (one wing-beat) vertical magnetic pulse generated by the two Helmholtz coils located on the floor and ceiling of the chamber. Such a short pulse is required to characterize the control mechanism on roll perturbations, since this degree of freedom is unstable on a time scale of a few wing-beats [14–18]. Controlling the voltage across the coils enables us to vary the magnetic field strength up to approximately 10^{-2} T, which is about 1000 times stronger than the Earth's magnetic field.

Since fruit flies fly with their body axis pitched up at approximately 45° and since the moment of inertia along their body axis is smaller than along the other axes (equations (2.1) and (2.2)), the largest deflection is generated along the body roll axis, with smaller perturbations along pitch and yaw (figure 1a,b).

2.3. Motion tracking

We analysed 20 sequences that span a perturbation range between 5° and 100°, in which the flies perform a steady flight before and after the correction manoeuvre. Using a custom image analysis algorithm [46], we extracted a three-dimensional kinematic description of the fly (figure 1) consisting of its body position and orientation (figure 1b) as well as the Euler angles (figure 1c) for both wings. Our motion tracking algorithm includes the following steps.

2.3.1. Pre-processing

Following background subtraction, we define two binary thresholds for each image: one for the darker body (without the wings) and one for the entire fly. In both side-view images, we automatically track and remove the fly's legs. In the top-view image, we segment the wings based on their motion by correlating a given frame with frames taken a quarter wing stroke (eight frames) before and after it. The motion-based segmentation is better than an intensity-based method, since a wing's intensity changes with the view angle and might appear as dark as the body. The pre-processing step results in seven binary images: a body-only image for each of the three views, two side-view images with the body and wings but without the legs, and a top-view image for each wing. Removing the legs and segmenting the wings is necessary to avoid self-occlusions in the three-dimensional hull reconstruction, which might result in fictitious wing-like protrusions in the reconstructed three-dimensional hull.

2.3.2. Hull reconstruction

Hull reconstruction is performed by dividing the filming volume into voxels and back-tracing each voxel to its corresponding pixel in each camera. A voxel is added to the three-dimensional hull if and only if its corresponding pixels values are 1 in all three views. We use a pinhole camera model to reconstruct three hulls. The three body-only images are used to reconstruct the body hull. The three-dimensional hull of each wing is obtained from its top-view image along with the two side-view images of the entire fly (with the legs removed).

2.3.3. Hull analysis

The body hull is used to find the body centre of mass and body Euler angles. An initial guess of the vector describing the body long axis is obtained from principal component analysis [46]. To reduce errors due to wing–body occlusions that add fictitious voxels to the body hull, we refine the initial guess by finding the positions of the body's anterior and posterior ends. These positions are calculated as the mean positions of 10% of the body voxels farthest from the body centre on each side. The body axis vector connects the anterior and posterior ends. The initial guess

for the body centre of mass position is then refined to be the midpoint of this line. The body axis vector is used to find the body yaw and pitch angles. The body roll angle was measured manually at the middle of every half stroke. In this measurement, we used the combined hull of body and wings to visually estimate the positions of the wing hinges and the body roll angle. Other methods based on the small angle between the fly's thorax and abdomen are prone to large errors [46]. The wing Euler angles were defined in the body frame of reference relative to the stroke plane (figure 1c). While in some insects, such as locusts, wing deformation is considerable and induces significant aerodynamic effects [50], in *D. melanogaster* wing flexibility is small and the aerodynamic forces are well described by a flat rigid wing [51]. Our measurements of *D. melanogaster* indicate that wing bending is negligible during most of the wing stroke and reaches no more than $5°$ during the wing's rapid (less than 0.3 ms) rotation between the down-stroke and up-stroke. Hence, in analysing the wing hull, we assume a flat rigid wing defined by its vein and chord vectors. We define the stroke plane using the body pitch angle of the fly before the perturbation, θ_b^0, which is typically $45°$. The stroke plane is defined in the body frame of reference by rotating the $\hat{x}_b\hat{y}_b$ plane by θ_b^0 degrees about the $\hat{y}_b$ axis. Thus, for example, if the fly body is pitched up by θ_b^0 and not rolled $\rho = 0$, the stroke plane coincides with the $\hat{x}\hat{y}$ plane in the laboratory frame of reference. We note that in previous work from our group the wing angles were defined in the laboratory frame [46]. In addition, here the stroke angle ϕ is defined as the angle between the projection of the wing-vein (leading edge) on the stroke plane and $\hat{h}_b$, which is the projection of the long body axis ($\hat{x}_b$) on the stroke plane (figure 1c). This definition better represents the wing actuation.

Finally, some of the movies were analysed manually. The results of these analyses showed very small differences when compared with results from the motion tracking algorithm.

2.4. Control experiments

We verified that flies without a magnet glued to their back were not affected by the magnetic field pulse. In addition, we verified that without an applied magnetic field, flies with a glued magnet flew similar to flies without a magnet. In particular, no statistical differences were observed in their heading, velocities and turning rates. Such results are not surprising since the change in mass is comparable to natural body weight fluctuations.

3. Results

3.1. Body and wing kinematics during roll correction manoeuvre

A representative example of a fly recovering from a $60°$ roll perturbation is shown in figure 1 and electronic supplementary material, movie S1. Body Euler angles, roll (ρ), yaw (ϕ_b) and pitch (θ_b), are plotted in figure 1e. The magnetic field was applied between $t = 0$ and 5 ms and induced a maximum roll velocity of $7000° \, \text{s}^{-1}$ resulting in a deflection of $60°$ within $t = 13.5$ ms (figure 1d, frame 3). The fly recovered its initial roll angle within 35 ms, or eight wing-beats. Top views show a clear asymmetry in wing stroke angles during the manoeuvre, which starts a single wing-beat (5 ms) after the perturbation (figure 1d, frames 1–4). During the manoeuvre, the left wing stroke amplitude increases, whereas the right wing stroke amplitude decreases. After some delay, the fly also spreads its legs from their folded position (frames 4–8) as in a typical landing response [52–54]. In addition, smaller deflections of $25°$ left in yaw and

$5°$ down in pitch were induced, as the applied torque is not completely aligned with a principal body axis (figure 1e).

The wing kinematics in terms of the wing Euler angles is shown in figure 2a–d. We quantify the asymmetry in wing kinematics by plotting the wing stroke angles during the manoeuvre (figure 2a). We find large differences (up to $70°$) between their peak-to-peak amplitudes (figure 2d). The amplitude asymmetry began one wing-beat after the onset of the perturbation, and lasted for five wing-beats. The flapping frequency of both wings remained nearly constant during the manoeuvre. Hence, to maintain the amplitude asymmetry, the left wing moved faster than the right (figure 2b). To first order, this difference in velocity leads to asymmetry in the aerodynamic forces of the two wings and generates a correcting torque.

The salient correction feature—a wing stroke-amplitude asymmetry with a response time of approximately one wing-beat—was observed in all the recorded events (figure 6a). The response time was both measured directly from wing kinematics as well as obtained from control model-fitting, as shown below. Moreover, this feature was robust to variability in initial flight pose and velocity. For example, the same mechanism was observed for hovering flies (electronic supplementary material, movie S2), flies with non-zero roll angle at the perturbation onset (electronic supplementary material, movie S3), and even for flies subject to two consecutive perturbing pulses (electronic supplementary material, movie S4, figures S3 and S4). Previous experiments with tethered flies associated stroke-amplitude asymmetry with roll correction manoeuvre [21,22]. This mechanisms has also been used for roll control in an insect-scale flapping robot [55].

3.2. Correcting torques

To calculate the aerodynamic torque generated by the insect, we used the full measured wing and body kinematics combined with a quasi-steady-state model for the aerodynamic force [51] produced by each wing. The calculated torques are similar for other quasi-steady-state force models [56,57] as well. The components of the aerodynamic torque vector along the $\hat{x}_b$ (roll) and $\hat{z}_b$ body axes were averaged over half-strokes and plotted in figure 2f,g (see figure 1c for axes definition). The torque magnitude is roughly 5 nN m and is comparable to torques exerted by tethered fruit flies [24]. Both the $\hat{x}_b$ and $\hat{z}_b$ torque components exhibit distinct peaks (solid circles) that appear simultaneously with the stroke-amplitude asymmetry.

The $\hat{x}_b$ component of the torque is easy to interpret since its only effect is to rotate the insect about the roll axis. The torque along the $\hat{z}_b$ axis acts to change all three Euler angles, because the insect flies with a finite body pitch angle of about $45°$. Figure 3 and electronic supplementary material, movie S6, give a specific example for this geometric effect, by showing the changes in body yaw, pitch and roll angles as a result of a geometric rotation along the $\hat{z}_b$ axis. The initial body orientation we used was the typical flight pose of the fly: $45°$ pitch up and zero roll. Figure 3 shows that for small rotations along $\hat{z}_b$, both the induced roll and yaw rotations are almost equal to the imposed $\hat{z}_b$ rotation. This observation implies that the torque that the fly exerts along the $\hat{z}_b$ axis has a comparable corrective effect on both yaw and roll. The full dynamics of the body rotations is described by the Euler equations of motion and is much more complicated and less intuitive than considering only rotations. The Euler equations have strong coupling
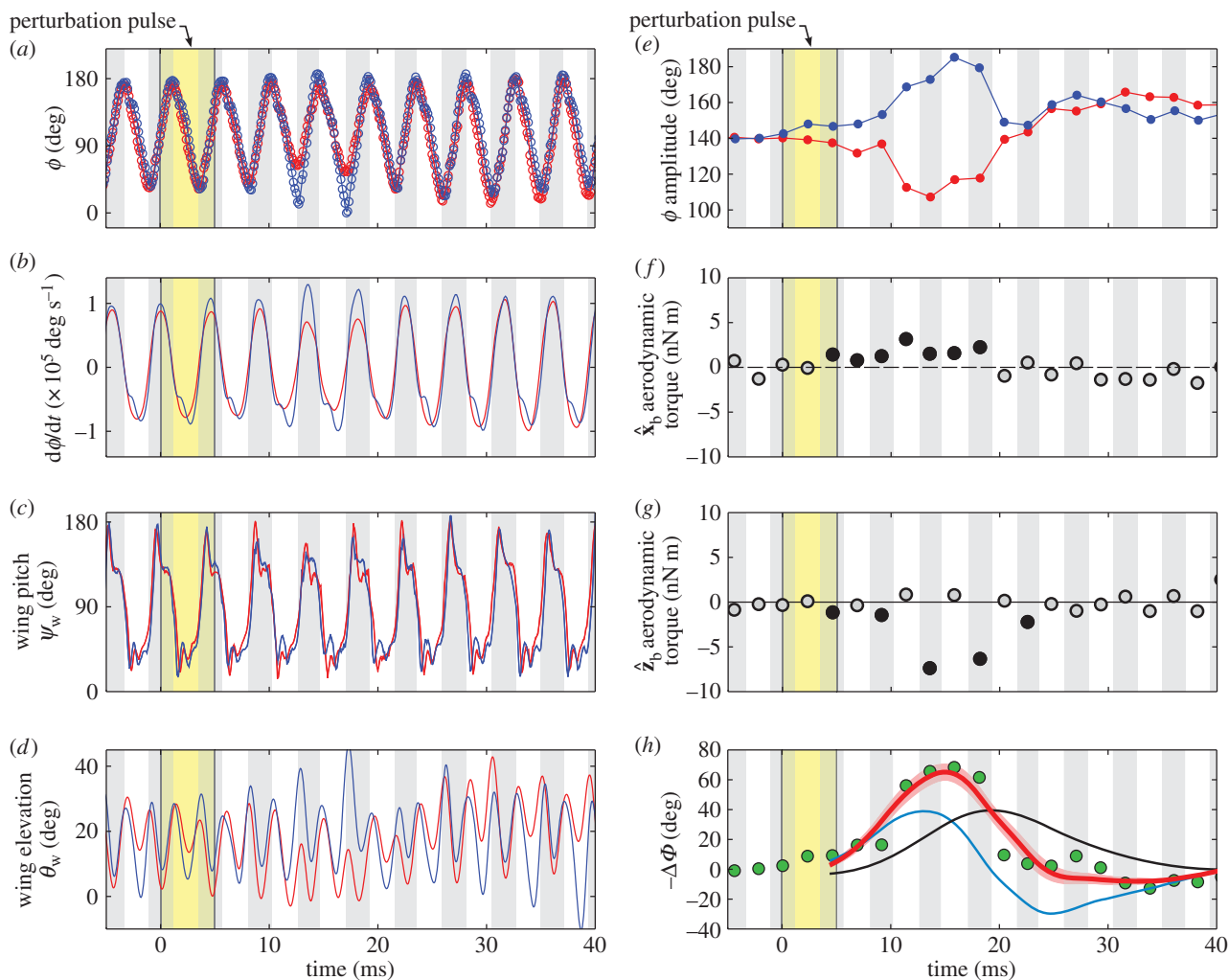
Figure 2. Roll correction mechanism for the manoeuvre in figure 1. Time is measured in milliseconds and the yellow stripe indicates the time of the magnetic pulse. White and grey stripes indicate forward and back stroke, respectively. In $(a-e)$, red indicates the right wing and blue indicates the left wing data. $(a-d)$ The wing Euler angles as a function of time. The angles are defined in the body frame of reference in figure 1c. (a) The stroke angles ϕ_w and (b) their angular velocity $\dot{\phi}_w$. (c) The wing pitch angles ψ_w. (d) The wing elevation angles θ_w. (e) The peak-to-peak amplitude of the stroke angles ϕ for each half-stroke. (f,g) Mean aerodynamic torque in each half stroke, calculated from the measured kinematics using a quasi-steady-state aerodynamic force model. Solid symbols highlight the correcting wing strokes. (f) The torque component along the body axis $\hat{x}_b$. Positive torque induces a corrective right roll, (g) the torque component along $\hat{z}_b$. Negative values have corrective effect. (h) Wing stroke amplitude difference $\Delta\Phi$ (green) and a PI controller fit (equation (3.1), red), with $\Delta T = 4.4 \pm 0.25$ ms, $K_p = 6 \pm 0.5$ ms and $K_i = 0.7 \pm 0.05$ (fitted values $\pm$ CI). The effect of the CI on the fitted curve is shown in shaded red. Contributions of the first and second terms of equation (3.1) are shown in blue and black, respectively. Measurement errors are comparable to the symbol size. (Online version in colour.)

between the components of the angular velocity, and become even more complicated when representing them in the Euler angles: yaw, pitch and roll. Nonetheless, the argument above gives a solid geometric intuition that a rotation along $\hat{z}_b$ has similar effects on yaw and roll.

The flies apply a torque along $\hat{z}_b$ during the backstrokes of the active part of the manoeuvre, and a torque along $\hat{x}_b$ during the forward strokes (figure 2f,g). The direction of the torque during a wing stroke cycle can be intuitively understood by a simple toy model (figure 4). We assume that the fly's body is pitched up by 45° and that during the middle of both the forward and back strokes the wings flaps with an angle of attack of 45°. The total aerodynamic force generated by a fly's wing, including both lift and drag, is typically perpendicular to the wing's surface, as has been characterized experimentally [51] and theoretically. At the middle of a forward stroke, the aerodynamic forces of both wings are parallel to $\hat{z}_b$ and their torque arm is along $\hat{y}_b$, which is parallel to the wing span direction. Hence, the force imbalance

resulting from the stroke-amplitude asymmetry induces a net roll torque along $\hat{x}_b$. Similarly, at the middle of a back stroke, the imbalanced aerodynamic forces from both wings are directed along $\hat{x}_b$ and their torque arm is still along $\hat{y}_b$, which induces a net torque along the $\hat{z}_b$ direction. Interestingly, this toy model implies that the fly cannot exert an exclusive correcting roll torque during the back strokes but, as shown above, the $\hat{z}_b$ torque has a corrective effect on both roll and yaw.

3.3. Control model

3.3.1. Fitting parameters for a proportional–integral control model

The response of the fly to the perturbation in terms of the wing stroke-amplitude asymmetry can be described by the response of a linear, PI controller

$$\Delta\Phi_{\text{model}}(t) = K_p \dot{\rho}(t - \Delta T) + K_i \rho(t - \Delta T). \qquad (3.1)$$
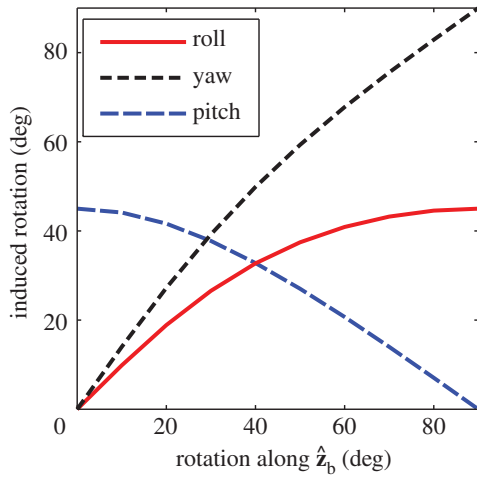
Figure 3. The effect of a rotation along the $\hat{\mathbf{z}}_b$ axis on the three Euler angles: roll (red), yaw (dashed black) and pitch (dashed blue). We assumed that the fly is initially posed at zero roll and pitched up by $45°$, and rotated it along its $\hat{\mathbf{z}}_b$ axis (see figure 1c for axis definition). The purely geometric calculation shows that a rotation along $\hat{\mathbf{z}}_b$ results in rotations along all three Euler angles. Specifically, for small rotations the magnitudes of the roll and yaw displacements are comparable. (Online version in colour.)

Here, the output $\Delta\Phi_{\text{model}}$ is the difference between the right and left wing stroke amplitudes, and the controller's input is the body roll velocity, $\dot{\rho}$, which flies measure using their rate-gyro sensor system associated with the haltere organs [21,58,59]. The controller is defined by three parameters: the proportional gain K_P, the integral gain K_i and a delay ΔT. Using the measured $\dot{\rho}$, ρ and $\Delta\Phi$, we fit for these three controller parameters. The procedure for parameter fitting and estimating their confidence intervals (CI) is detailed in the electronic supplementary material.

The control block-diagram of the fly and its roll-perturbation controller is shown in figure 5. The input signal of the controller is the roll angular velocity measured by the haltere sensors (S) and delayed by ΔT. The controller output $\Delta\Phi$ is an actuation signal converted by the wings (W) into the counter-torque exerted by the fly (figure 6b). The counter-torque is opposite to the external perturbation torque τ_{ext}, thereby forming a negative feedback loop, which is crucial for roll correction. The corrective nature of the aerodynamic torque exerted by the fly is shown in figures 2–4 and 6.

The same control model could have been called a PD model (proportional–derivative) with its input signal being the roll angle ρ rather than $\dot{\rho}$. In a PD model, the proportional term would consist of the roll angle and the derivative term would consist of the roll velocity, resulting in an identical form to equation (3.1). We chose the PI terminology for this model to emphasize that the fly measures its angular velocity and integrates this signal to obtain roll displacement. Note that the PI controller model determines the roll displacement by integrating the roll velocity. Hence, the controller alone cannot determine the absolute roll angle and can elicit correction of roll displacements with respect to a pre-perturbation reference roll angle (see Discussion).

Fitting the PI model to the manoeuvre in figures 1 and 2, we find that this controller response (red curve, figure 2g) is sufficient to reproduce the time-dependence of $\Delta\Phi$ (green circles). The fitted parameters are $\Delta T = 4.4 \pm 0.25$ ms, $K_P = 6 \pm 0.5$ ms and $K_i = 0.7 \pm 0.05$ (values $\pm$ CI), with $R^2 = 0.9$ for
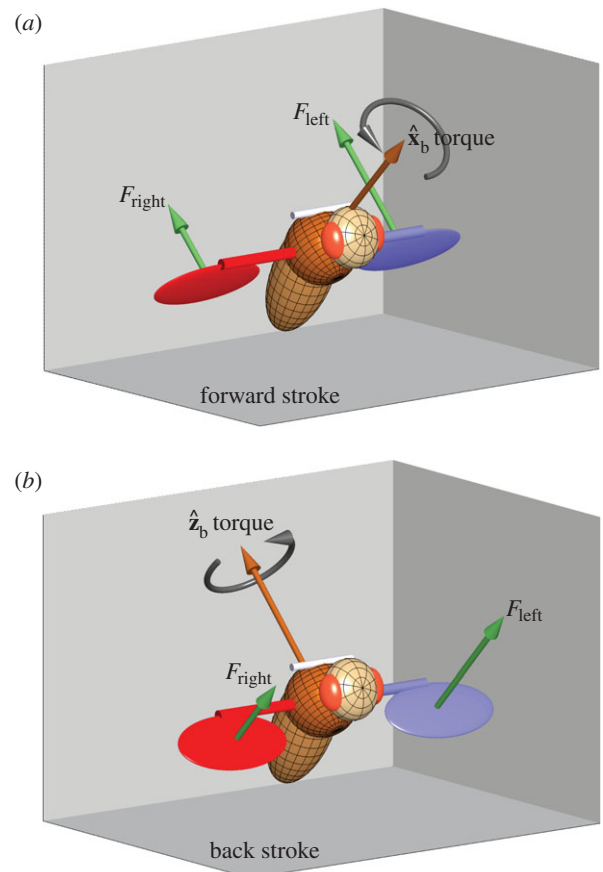

Figure 4. A toy model for torque production. Consider a fly with a body pitch angle of $45°$ and applying a stroke-amplitude asymmetry, such that its left wing (blue) exerts a larger aerodynamic force than its right wing (red) $F_{\text{left}} > F_{\text{right}}$. The aerodynamic forces (green arrows) are perpendicular to the surface of each wing. (a) During the middle of a forward stroke, the wings are assumed to flap with an angle of attach of $45°$, hence the aerodynamic forces are perpendicular to the body $\hat{\mathbf{x}}_b$ (roll) axis. Since their torque arms are along the span vector, which is parallel to the $\hat{\mathbf{y}}_b$ body axis, the net aerodynamic torque is along $\hat{\mathbf{x}}_b$. The torque is exerting a roll acceleration to the right. (b) During the middle of a back stroke, we also assume an angle of attack of $45°$, which implies that the aerodynamic forces are perpendicular to the $\hat{\mathbf{z}}_b$ body axis. The torque arms are still along $\hat{\mathbf{y}}_b$, hence the net torque is along the $\hat{\mathbf{z}}_b$ axis. The net torque has a combined effect on the body Euler angles, including roll right, yaw right and pitch down as shown in figure 3.
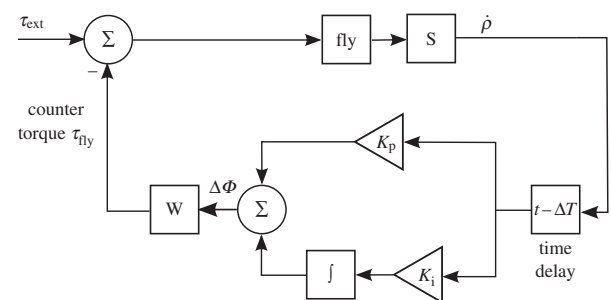

Figure 5. Control block-diagram. The fly's dynamics is described by the fly block and the haltere sensors (S) measure its roll velocity $\dot{\rho}$. The $\dot{\rho}$ signal is fed into a time-delay block that represents a neuromuscular response time. The delayed signal is then split into two branches: the proportional term with the K_P coefficient and the integral term with the K_i coefficient. The sum of both terms gives the actuation signal $\Delta\Phi$, also described in equation (3.1). The actuation signal is converted by the wings (W) into the counter-torque exerted by the fly. The counter-torque is opposite to the external perturbation torque τ_{ext}, thereby forming a negative feedback loop that eventually corrects for the external perturbation.
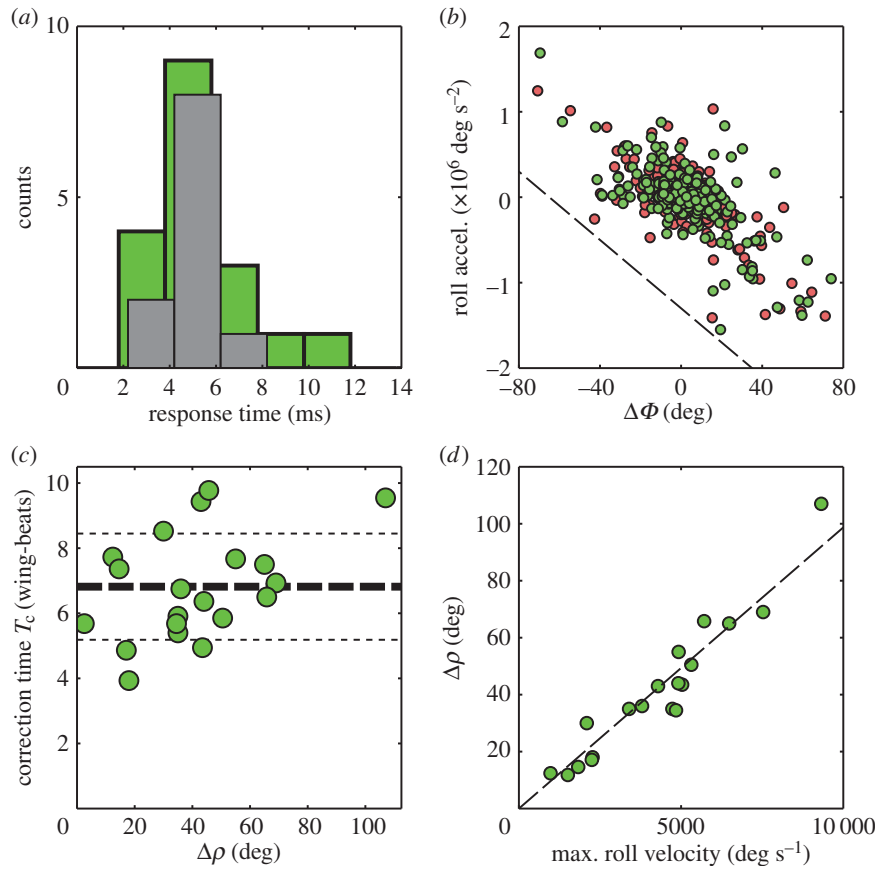
Figure 6. (*a*) Response time histograms for multiple perturbation events: delay time of fitted PI controllers ($n = 11$, dark grey) and the time to reach $\Delta\Phi = 10°$ measured from wing kinematics ($n = 20$, green). Histograms are shifted to improve visibility. (*b*) Mean roll acceleration versus $\Delta\Phi$ for 299 forward strokes (red) and 304 back strokes (green). The correlation coefficient of these two quantities is -0.67 (*p*-value $< 10^{-12}$). The dashed line has a slope of $-20 \times 10^3 \ \text{s}^{-2}$. (*c*) Roll correction time T_c measured in wing-beats as a function of $\Delta\rho$ for 20 events. The mean correction time (thick dashed line) is 6.8 ± 1.6 wing-beats (mean $\pm$ s.d.). Thin dashed lines indicate 1σ margins. (*d*) Maximum roll displacement $\Delta\rho$ as a function of the maximum roll angular velocity for 20 events. The dashed line has a fitted slope of 9.9 ms with a 95% confidence interval of ± 0.75 ms. (Online version in colour.)

the fit. Notably, the response time is comparable to a single wing-beat, consistent with the direct measurement of the wing kinematics (figures 1, 2 and 6*a*). The fast rise time can be attributed to the term proportional to the roll velocity (figure 2*g*, blue curve). The fitted curve is insensitive to variations within the CI (figure 2*g*, shaded red). Similar results are shown in electronic supplementary material, figure S3, for a movie in which the fly was subject to a double-pulse perturbation.

In-depth analysis of 11 correction manoeuvres showed the $\Delta\Phi$ response is consistent with the PI controller model (table 1, mean $R^2 = 0.86$). Fitting control parameters for each manoeuvre separately, we find $K_p = 4.8 \pm 2.4$ ms and $K_i = 0.6 \pm 0.3$ (mean $\pm$ s.d.). The mean response time $\Delta T = 4.6 \pm 1$ ms is comparable to a single wing-beat period (figure 6*a*). The confidence intervals for parameters in each event are smaller than the standard deviation, indicating that differences between fitted controllers can be attributed to natural variation between flies (table 2).

Table 1. Fitting results for the PI control model, including confidence intervals (CI) for the fitted parameters.

movie	$\Delta T \pm$ CI (ms)	$K_p \pm$ CI (ms)	$K_i \pm$ CI	R^2
1	4.4 ± 0.25	6.0 ± 0.5	0.70 ± 0.05	0.90
2	4.6 ± 1.0	2.5 ± 0.7	0.35 ± 0.03	0.80
3	3.6 ± 0.3	3.5 ± 0.5	0.90 ± 0.05	0.91
4	4.4 ± 0.4	4.0 ± 1.0	0.70 ± 0.12	0.76
5	5.1 ± 0.3	5.0 ± 0.5	0.50 ± 0.05	0.96
6	5.3 ± 1.0	2.5 ± 0.5	0.10 ± 0.05	0.83
7	5.6 ± 0.3	8.5 ± 0.6	0.25 ± 0.10	0.86
8	2.6 ± 1.0	2.0 ± 1.0	0.75 ± 0.07	0.87
9	4.3 ± 0.5	4.5 ± 1.0	0.95 ± 0.06	0.77
10	6.7 ± 0.6	9.5 ± 0.8	0.15 ± 0.10	0.91
11	4.1 ± 0.6	5.0 ± 0.6	0.85 ± 0.15	0.86

3.3.2. Alternative proportional–integral–differential control models

Prior literature has shown that flies do not show a significant response to angular accelerations but do sense and respond to angular velocities via the haltere organs [21]. These observations suggest control models that do not use angular

acceleration as an input (the differential term in PID, see §4.3 as well as in electronic supplementary material). In the framework presented here, this restricts our models to those containing only the terms proportional to the angular velocity (P) or its integral the angular displacement (I).

Table 2. Mean variation of the PI controller parameters.

parameter	ΔT	K_p	K_i
mean ± s.d.	4.6 ± 1.0 ms	4.8 ± 2.4 ms	0.6 ± 0.3
mean CI value	0.57 ms	0.66 ms	0.08
s.d./CI ratio	1.75	3.64	3.75

Table 3. Fitting results for three linear control models.

model	functional form	r.m.s.e.
PI	$\Delta \Phi(t) = K_p \dot{\rho}(t - \Delta T) + K_i \rho(t - \Delta T)$	6.7°
P	$\Delta \Phi(t) = K_p \dot{\rho}(t - \Delta T)$	16.4°
I	$\Delta \Phi(t) = \quad\quad\quad\quad K_i \rho(t - \Delta T)$	10.5°

Table 4. Fitting results for three linear control models for the movie in figures 1 and 2.

model	ΔT (ms)	r.m.s.e. (°)	R^2
PI	4.4	8.7	0.90
P	6.9	20	0.47
I	0.0	14	0.74

For completeness, we also fit the data with two simpler control models. We tested an integral-only (I) controller and a proportional-only (P) controller by fitting them to the measured $\Delta \Phi$ as described above (table 3). The metrics used to assess the controller fit are R^2 and the root-mean-square error (r.m.s.e.) of the difference between the measured $\Delta \Phi$ and the value predicted by the control model, averaged across the movies in our dataset (tables 3 and 4). As expected, because the PI model includes both P and I models, it fits the data better with a lower r.m.s.e. value and higher R^2 value. However, the subset models can be rejected based on more substantial reasons. The P-controller is unrealistic, since it does not contain the roll angle, which is the quantity the fly is evidently controlling. Specifically, a P-controller would bring the fly to zero angular velocity but at an arbitrary roll angle. The I-controller is also unrealistic, since its best fits yielded latency times that are too short for an animal, between 0 and 0.3 ms. Table 4 shows an example for the manoeuvre in figures 1 and 2, in which the fitted time delay $\Delta T = 0$ is unfeasible. The I-controller requires such a short latency because the roll angle (I-term) peaks later than the roll velocity (figure 2g; electronic supplementary material, figure S4f), which forces the I-controller to respond almost immediately. In summary, the P-term is required to explain the observed latency, and the I-term is required since it represents the controlled quantity. Together, they combine to produce a PI controller, which seems to be a minimal model for the roll-perturbation controller.

3.3.3. Hallmarks of linear control

To further illustrate that wing asymmetry generates corrective roll dynamics, we determine the mean roll acceleration for approximately 600 half-strokes and plot it versus $\Delta \Phi$ (figure 6b). The $\Delta \Phi$ asymmetry is negatively correlated with the roll acceleration generated by the fly, such that $\Delta \Phi$ generates a counter-torque that forms a negative feedback with a corrective effect for the roll perturbation. Thus, for example, negative $\Delta \Phi$ is correlated with positive roll acceleration (figures 1 and 2; electronic supplementary material, figures S3 and S4). Thus, while the controller output is computed in terms of $\Delta \Phi$, figure 6b shows that $\Delta \Phi$ is proportional to roll acceleration, which in turn enables the fly to control the roll angle.

The data also show two hallmarks of linear control. First, the correction time is insensitive to the maximum roll deflection, $\Delta \rho$. Here, the correction time T_c is the time between onset of the perturbation and the moment when the roll angle reaches 10% of $\Delta \rho$. Plotting T_c as a function of $\Delta \rho$ shows the correction time is 6.8 ± 1.6 wing-beats (mean ± s.d., $n = 20$) with little dependence on perturbation amplitude (figure 6c). Second, we find that $\Delta \rho$ increases linearly with maximum roll velocity (figure 6d). Collectively, these

data suggest that, as with yaw [39], the response to roll perturbations is well described by a reduced order model of a linear PI controller with time delay.

3.4. Evidence for prioritized control

The perturbing torque was horizontal and not aligned with a principal body axis, since a fly's typical body pitch angle is 45°. The torque induced the largest angular deflection along the body roll axis and secondary deflections along the other body axes. In particular, we found that both the yaw angle and the direction of the body velocity were altered significantly. In yaw, we find that when the fly is rolled to its right there is a corresponding rightward yaw deflection and vice versa (figure 7a). Maximum yaw deflection was observed at the same time as the maximum roll deflection, about four wing-beats after the onset of the perturbation. Across our entire dataset, the maximum yaw deflections increase roughly as $\approx (1/2) \Delta \rho$ with significantly greater scatter at large $\Delta \rho$.

In contrast to previous experiments where perturbations were restricted to yaw and were corrected with small errors [39], here we observed that the secondary deflections along the yaw and body velocity orientations were often left partially uncorrected (figure 7b,c). A typical example of a fly perturbed during forward flight is shown in figure 7a by a superposition of top-view images. Following the external torque, the fly was deflected by 45° leftward along the roll axis, 30° leftward in yaw and 5° down in pitch. As indicated by the flight trajectory, while the fly fully corrected its roll angle with $T_c = 6.5$ wing-beats, deflections of 8° in yaw and 15° in the direction of the body velocity persisted until the end of the measurement. From previous experiments [39], we know that a yaw-only perturbation of 30° should have been corrected within 14 wing-beats to 2° accuracy. In the current experiment, however, larger residual deflections ('error') in yaw and the velocity heading persist long after 14 wing-beats (see label in figure 7a).

Figure 7b shows the yaw 'errors' as a function of the imposed yaw deflection for multiple perturbation events. The yaw 'errors' were measured at $t = 11$ wing-beats, a time by which the roll manoeuvre has already ended, and we did not observe any other distinct manoeuvres for yaw correction. The plot shows yaw 'errors' larger than 10% of
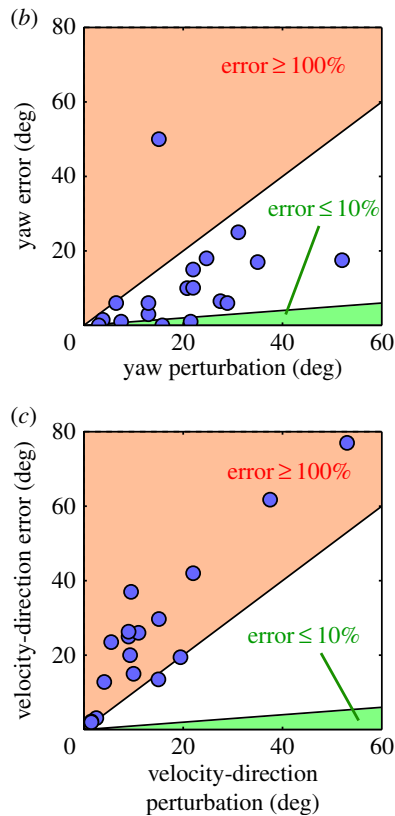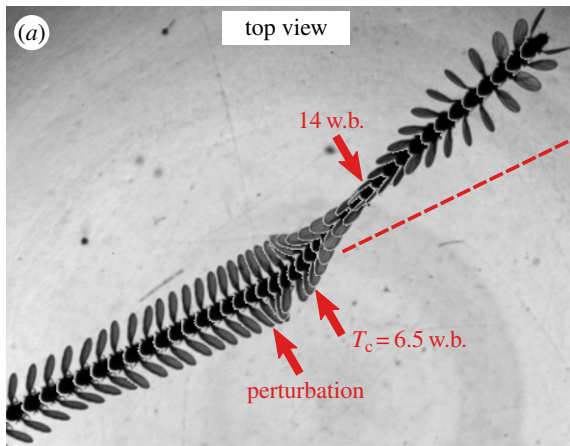
Figure 7. (a) Superimposed top-view images of a typical roll correction manoeuvre following a perturbation of $\Delta\rho = 45°$ leftward in roll, 30° leftward in yaw and 5° down in pitch. The perturbation time $t = 0$, correction time T_c, and $t = 14$ wing-beats are indicated by red arrows. The fly moved from left to right and the snapshots were taken every 4.5 ms. After roll has been corrected, the fly continued in a straight trajectory with uncorrected differences of 8° in yaw and 15° in the velocity heading. The 7° difference between the two angles is attributed to small side-slip motion before the perturbation, such that the fly's velocity was misaligned with its yaw angle. The dashed red line illustrates a hypothetical unperturbed trajectory. (b) Yaw difference ('error') between $t = 0$ and 11 wing-beats as a function of the maximum yaw perturbation. The 11 wing-beat time is after the roll manoeuvre has ended and also corresponds to the time in which approximately 10% yaw error is achieved after yaw-only perturbations. The green area represents 'error' less than or equal to 10%. The orange area above the unity slope represents an increase of the perturbation. (c) A similar plot for the direction of the body velocity. (Online version in colour.)

the imposed yaw perturbation (above the green region in figure 7b). Remarkably, a similar plot for the 'errors' in the body velocity direction at 11 wing-beats shows that they are even larger than the imposed perturbation to the body

velocity orientation (orange area in figure 7c). Thus, the velocity orientation was not even partially corrected. Instead, its deflection increased during the roll correction. The qualitatively different yaw response with and without the roll deflection hints that the fly prioritizes roll correction while compromising other angles.

3.5. Extreme perturbations
3.5.1. Experimental measurement
To test the linear control model for roll, we challenged the flies with extreme perturbations in which they were spun multiple times in mid-air by a series of magnetic pulses. The fly shown in figure 8a and electronic supplementary material, movie S5, was rotated eight times to its right. The accumulated roll angle exceeded 3000° (figure 8b) and the maximum roll velocity was over 60 000° s^{-1} (figure 8c). During the perturbation, the fly was unable to oppose the magnetic torque. In fact, the right wing, which in a typical correction manoeuvre flaps with a larger stroke amplitude, hardly flapped at all and occasionally seemed disconnected from its flight power muscles. We captured three such events, all showing the same behaviour. Remarkably, once the magnetic pulses stopped, the flies regained control within three to four wing-beats. The response of flies to such extreme perturbation can shed light on the validity limits of the linear control model and provide hypotheses regarding nonlinear features of the flight controller.

The response to these extreme perturbations indicates that flies are able to come back to nearly zero roll angle independently of the number of imposed revolutions along roll. While a linear PI controller model well describes the response of flies to single-impulse perturbations, this model cannot account for the response to extreme perturbations. Under such perturbations, the integral term of the PI controller should have accumulated a signal corresponding to a 3000° deflection. This signal would both saturate the actuation response of $\Delta\Phi$ and, more importantly, the resulting correction manoeuvre would require the fly to rotate 3000° in the opposite direction. Clearly, flies circumvent this scenario. While the strategy the flies use is not clear, we hypothesize that above some perturbation amplitude the roll controller switches from a linear PI to another control behaviour that should include two mechanisms. The first mechanism would limit or reset the value of the integral term. In control theory such an operation is termed integral 'anti-windup'. The second mechanism would employ an additional sensory modality that measures the direction of gravity independent of the halters to correct for roll. It is plausible that in such manoeuvres the time scales are long enough that flies may be able to incorporate such an additional sensory modality.

3.5.2. Passive versus active damping
Our calculations show that roll deceleration is only explained by active flapping, rather than passive aerodynamic damping due to the wings. To estimate the role of passive aerodynamic damping in the recovery of fruit flies from extreme perturbation, we calculated an upper limit for the damping during the manoeuvre shown in figure 8. The upper limit was estimated by considering a fly rolling along its long axis ($\hat{x}_b$) with its wings static with respect to the body and maximally stretched sideways with $\phi = 90°$ and $\psi = 45°$ (figure 9, inset). This configuration, in which the normal to

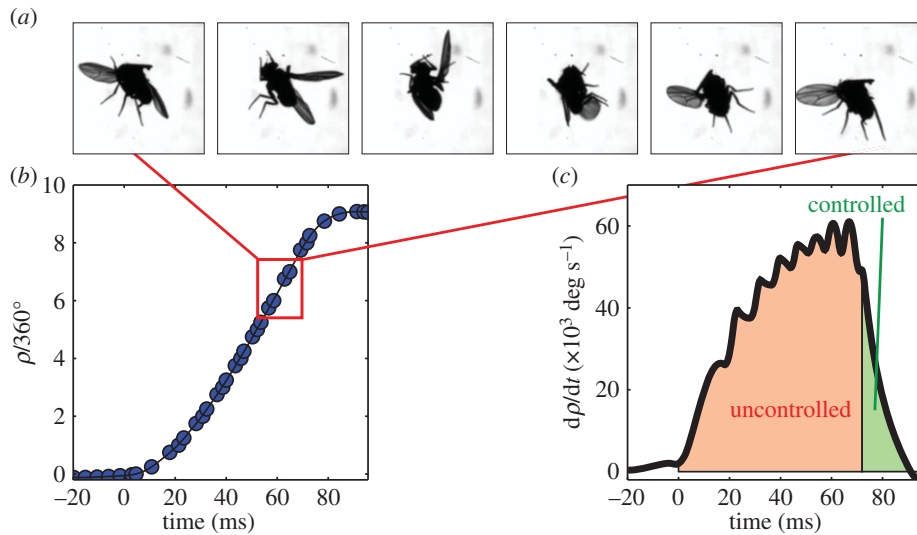**Figure 8.** Extreme perturbation. (*a*) Snapshots, taken 1.25 ms apart, of a fly being rotated clockwise at approximately $60\,000°\,\mathrm{s}^{-1}$ by a pulse train of magnetic torques. (*b*) Roll kinematics during the manoeuvre (blue circles), and its smoothing spline (black line). The perturbation was on between $t = 0$ and 72 ms. Measurement errors are smaller than the symbol size. (*c*) Roll velocity versus time (black line). The fly was unable to control its flight during the perturbation (orange shading, uncontrolled) and actively corrected roll once the perturbation stopped (green shading, controlled). The fly levelled itself to $\rho = 20°$ within four wing-beats after the perturbation stopped, towards $\rho = 0$. (Online version in colour.)
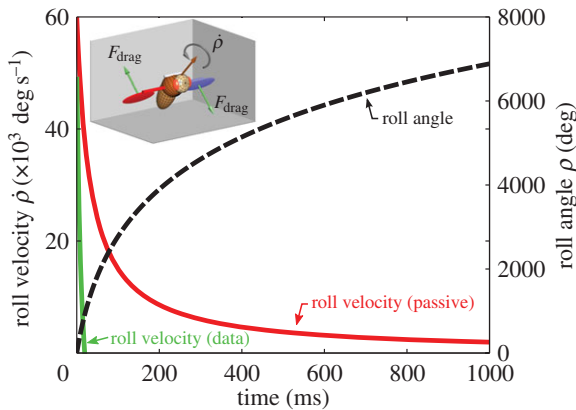

Figure 9. The contribution of passive roll damping to the recovery from a roll extreme perturbation. Plotting the calculated dynamics of the roll velocity (red) and roll angle (dashed black line) under passive aerodynamic damping. The measured data for the roll velocity are copied from figure 8*c* (green). The calculation assumed an upper limit for the damping torque. The initial condition consisted of a roll velocity of $60\,000°\,\mathrm{s}^{-1}$ as in the experiment described in figure 4, and zero roll angle at $t = 0$. The slow approximately $1/t$ decay of the roll velocity indicates that passive damping alone cannot explain the fast recovery observed in the experiment. Inset shows the configuration of the rotating fly. The fly is rotating about its roll axis (orange) and each wing is pitched to $\psi_\mathrm{w} = 45°$ such that its angle of attack with respect to the ambient air is $90°$. The green arrows indicate the aerodynamic drag forces on each wing.

the wing surface is parallel to the wing's velocity induced by body rotation, achieves maximum drag that passively damps the rotation along roll. The aerodynamic drag force F_drag on each wing was calculated using a quasi-steady-state force model [51,60] of the form

$$F_\mathrm{drag} = \frac{1}{2}\rho_\mathrm{air}\,S\,\hat{r}_2^2\,C_\mathrm{D}\,U_\mathrm{tip}^2. \tag{3.2}$$

Here, ρ_air is air density, S is the wing area, $\hat{r}_2^2$ is a dimensionless shape factor, C_D is the drag coefficients determined

experimentally using a scaled-up model of a fruit fly wing [51] and U_tip is the velocity of the tip of the wing. The aerodynamic torque of the two wings is $\tau = 2LF_\mathrm{drag}$, where L is the torque arm with respect to the body centre-of-mass, corresponding to the body radius plus 2/3 of the wing span (centre-of-pressure position). We solve the equation of motion for roll: $\ddot{\rho} = \tau/I_{xx}$, with the initial condition $\dot{\rho}(0) = 60\,000°\,\mathrm{s}^{-1}$ corresponding to the end of the external perturbation in the experiment (figure 8), and $\rho(0) = 0$, which was arbitrarily chosen.

The solution for $\dot{\rho}(t)$ and $\rho(t)$ (figure 9) shows that their decay is much slower than in the observed recovery manoeuvre (figure 8). While in the experiment the fly managed to completely brake its roll velocity approximately 25 ms after the perturbation torques had ended, by this time the passively damped model slowed down only to approximately $30\,000°\,\mathrm{s}^{-1}$, which is half its initial velocity. The scaling of the $\dot{\rho}$ decay is obtained from its equation of motion that has the form $\mathrm{d}\dot{\rho}/\mathrm{d}t \propto (\dot{\rho})^2$. Its solution decays slowly as $1/t$, such that even by $t = 1000$ ms the roll velocity is $2000°\,\mathrm{s}^{-1}$ and the roll angle has completed almost 20 rotations (figure 9). These calculations show that, while it may be useful in slowing down at short times, passive damping alone cannot account for the corrective torques and active torque generation must be considered. Since the maximum wing stroke angular velocity (figure 2*b*) is approximately twice as fast as the imposed roll velocity of $\dot{\rho}_\mathrm{o} = 60\,000°\,\mathrm{s}^{-1}$, the corrective torque due to flapping is much larger than passive damping: the two wings experience rotation equivalent to $3\dot{\rho}_\mathrm{o}$ and $\dot{\rho}_\mathrm{o}$, respectively, and since the aerodynamic force is quadratic in the wing's airflow, the maximum active braking torque could be estimated to be approximately $3^2 + 1^2 = 10$ times larger than passive damping.

While the above calculation was done for the extreme, multiple rotation, perturbation, it is even more relevant for slower perturbations in the 'linear regime' (figures 1–4), since the damping force is quadratic in the wing velocity and, hence, even less significant.

4. Discussion

4.1. Response time of the roll correction reflex

The average response time of the roll reflex is 5 ms (a single wing-beat). The response time is defined as the time from the onset of the perturbation until a stroke-amplitude asymmetry of $\Delta\Phi = 10°$ was detected (figure 6a, green). A similar response time was obtained from fitting the PI controller (figure 6a, grey and table 1). The onset of the perturbation was chosen as a reference time for the response. Importantly, here we measure a behavioural response time, from a stimulus to a mechanical action. This measurement is distinct from measurements of the neural response time, from a stimulus to the activation of a given neuron in the response pathway. The behavioural response typically requires the collective action of sensory neurons, inter-neurons and motor neurons to elicit a measurable mechanical behaviour.

The roll reflex is 3.5 times faster than the response of fruit flies to yaw perturbations [39] and 2.5 times faster than their response to pitch perturbations [13]. These differences highlight the relative importance of roll control. The roll response is also five times faster than visual startle response in flies (25 ms) [61] and the entire correction manoeuvre is completed before the flies can elicit a visual response.

The 5 ms response time places this reflex among the fastest behavioural reflexes in the animal kingdom. It is comparable to the head-roll compensation reflex in blowflies (5–7.5 ms) [25], the startle response in teleost fish (5–10 ms) [47,62], the mandible strike of trap-jaw ants (4–10 ms) [63] and the escape response of cockroaches (11–18 ms) [64,65]. Among these animals, the fruit fly is by far the most studied and experimentally accessible organism, which opens the way for studying the neurobiology of roll control as a model system for extremely fast reflexes.

4.2. The duration of the correction manoeuvre

Our data show that 90% of the roll perturbation is corrected within 30 ± 7 ms (6.8 ± 1.6 wing-beats). The correction time is comparable to the flies' visual response time of 25–30 ms [61], implying that flies do not use their compound eyes during roll correction. This observation is consistent with previous studies on the integration of haltere and visual signals in tethered flies, showing temporal filtering of rotational information: the visual system is used to measure slow rotations while the halteres are used to measure fast rotations [22,23].

4.3. Stroke-amplitude asymmetry

The wing stroke-amplitude asymmetry measured in our experiments reaches approximately $80°$, as shown, for example in figures 1d and 2; electronic supplementary material, figures S3b, S4 and movies. This asymmetry is significantly larger than the maximum asymmetry of 10–15° measured in experiments with tethered flies that were rotated inside a gimbaled apparatus [21]. The difference in the maximum asymmetry can be attributed to the different magnitude of the roll perturbations in the tethered experiments and the free-flight experiments reported here, both in terms of the angular displacement and angular velocity. The maximum angular displacement obtained in tethered experiments was $30°$ [21–23], while the current free-flight experiments reach $100°$ (figure 6c,d). The maximum angular velocity in the tethered experiments was $800° \, \mathrm{s}^{-1}$ [21–23], compared with $9400° \, \mathrm{s}^{-1}$ in the free-flight experiments (figure 6d). The smaller velocity in the tethered preparations stems from the large inertia of the rotating gimbaled apparatus. In addition, the imposed rotations in the tethered experiments were oscillatory with a characteristic period of approximately 1 s, while the mid-air perturbations were torque impulses of only 5 ms. Since the fly's halteres sense angular velocity and the maximum angular velocity perturbations were more than 10 times faster in the free-flight experiments, it is plausible that the reason for the larger wing stroke asymmetry response was simply the stronger stimuli.

To check this conjecture, we used the PI controller model to predict the roll response of tethered fruit flies previously published by Dickinson [21]. In one of these tethered experiments, flies were mounted on a gimbaled apparatus oscillating along the roll axis with an amplitude $25°$, a period of 0.6 s, and a maximum velocity of $250° \, \mathrm{s}^{-1}$. Importantly, the flies had no visual cues relating to the imposed rotation. As shown in the electronic supplementary material, figures S4 and S5, we find that the PI control model well describes the response data ($R^2 = 0.8$). Moreover, the PI control model shows that the response of the fly is independent of its roll acceleration, supporting a PI rather than a PID control model (electronic supplementary material, figure S6). We do find that the values of the controller parameters fitted for the tethered experiment are different from the controller parameters fitted to the free-flight experiment reported here (table 2). Possible reasons for this difference are natural variability among flies (as characterized by the free-flight data) as well as the different experimental methods: using tethered compared to free flying animals. Finally, since the tethered flies did not have any visual cue about the imposed rotation, the data strongly suggest that the fly's roll response is mediated by the haltere-based mechanical sensors, consistent with the PI control model.

4.4. The PI controller model

The PI controller model determines the roll displacement by integrating the roll velocity. This controller alone cannot determine the absolute roll angle. Hence, we hypothesize that to avoid accumulation of errors while integrating the haltere angular velocity readout, the fly may be adjusting the reference roll angle by combining information from another sensory modality, such as the compound eyes or ocelli. Owing to the known temporal filtering the fly applies to the rotational information it acquires—using the haltere readout in its response to fast rotations and the visual system in its response to slow rotations [22,23]—we conjecture that the PI controller model describes a reflexive response to the fast perturbations applied in our experiments, while adjusting the absolute roll angle at a slower time scale using the visual system. Our measurements of the fly's response to extreme perturbations, where the fly seems to know where 'down' is although its roll integrator most probably saturates, are consistent with this hypothesis, since these manoeuvres are long enough to allow an incorporation of information from slower sensors.

4.5. Comparing roll and yaw control

Although the control mechanisms for body roll and yaw [39] are mathematically equivalent, there are substantial

differences between these two degrees of freedom and the fly's response to perturbations along these angles. First, roll is an unstable degree of freedom while yaw is stable. Moreover, in yaw, the perturbation velocity is passively damped to half its value after only two wing-beats [66]. Second, if a roll perturbation is not fully corrected the fly will start turning and losing altitude, whereas in yaw, if a perturbation is not fully corrected the fly can keep flying only in a different direction. Third, the one wing-beat response time of the fly to roll perturbation is 3.5 times faster than the yaw response time. Together, it is clear that controlling roll perturbations is more challenging than controlling yaw perturbations.

4.6. Hypothesized nonlinear control architecture under complex perturbations

An open problem arising from our study is understanding the structure of the overarching controller for all the body angles. When modelling the control system, treating roll separately from yaw is justified by the much faster time scales of the response and correction associated with roll. As previously measured in [39], the response time of fruit flies to yaw-only perturbations is 3.5 wing-beats (17.5 ms), whereas their response time to the perturbations in the current study is only one wing-beat (5 ms and sometimes even less). In the current experiments, by $t = 17.5$ ms, the flies have already been actively correcting roll for 2.5 wing-beats. Beyond $t = 17.5$ ms, we do not see any different correction manoeuvre that may indicate the onset of yaw correction. As mentioned above, the the $\hat{z}_b$ torque pulses have some corrective effect on yaw; however, the onset time of these torques suggests they are a part of the roll manoeuvre. In addition, we observe sizeable residual deflection in yaw, long after the roll correction is finished and also long after any hypothetical yaw correction should have been performed. These results show that roll and yaw are, indeed, coupled: rather than fully correcting for both angles at the same time, it seems that flies prioritize roll correction over yaw. This may be another reason that explains why the decoupled roll-only controller well approximates the observed response. To map out the full controller, it will be necessary to measure the insect's response to sophisticated perturbations along multiple axes, whose direction, amplitude and timing are individually controlled. Such measurements will further reveal the strategies insects use to manage their actuation resources and achieve the grace and performance of their flight.

References

1. Combes SA, Dudley R. 2009 Turbulence-driven instabilities limit insect flight performance. *Proc. Natl Acad. Sci. USA* **106**, 9105–9108. (doi:10.1073/pnas.0902186106)

2. Ravi S, Crall JD, Fisher A, Combes SA. 2013 Rolling with the flow: bumblebees flying in unsteady wakes. *J. Exp. Biol.* **216**, 4299–4309. (doi:10.1242/jeb.090845)

3. Ortega-Jimenez VM, Greeter JS, Mittal R, Hedrick TL. 2013 Hawkmoth flight stability in turbulent vortex streets. *J. Exp. Biol.* **216**, 4567–4579. (doi:10.1242/jeb.089672)

4. Vance J, Faruque I, Humbert J. 2013 Kinematic strategies for mitigating gust perturbations in insects. *Bioinspir. Biomim.* **8**, 016004. (doi:10.1088/1748-3182/8/1/016004)

5. Sane SP. 2003 The aerodynamics of insect flight. *J. Exp. Biol.* **206**, 4191–4208. (doi:10.1242/jeb.00663)

6. Wang ZJ. 2005 Dissecting insect flight. *Annu. Rev. Fluid Mech.* **37**, 183–210. (doi:10.1146/annurev.fluid.36.050802.121940)

7. Taylor GK, Thomas AL. 2003 Dynamic flight stability in the desert locust *Schistocerca gregaria*. *J. Exp. Biol.* **206**, 2803–2829. (doi:10.1242/jeb.00501)

8. Sun M, Xiong Y. 2005 Dynamic flight stability of a hovering bumblebee. *J. Exp. Biol.* **208**, 447–459. (doi:10.1242/jeb.01407)

9. Taylor GK, Żbikowski R. 2005 Nonlinear time-periodic models of the longitudinal flight dynamics of desert locusts *Schistocerca gregaria*. *J. R. Soc. Interface* **2**, 197–221. (doi:10.1098/rsif.2005.0036)

10. Sun M, Wang J, Xiong Y. 2007 Dynamic flight stability of hovering insects. *Acta Mech. Sin.* **23**, 231–246. (doi:10.1007/s10409-007-0068-3)

11. Liu H, Nakata T, Gao N, Maeda M, Aono H, Shyy W. 2010 Micro air vehicle-motivated computational biomechanics in bio-flights: aerodynamics, flight dynamics and maneuvering stability. *Acta Mech. Sin.* **26**, 863–879. (doi:10.1007/s10409-010-0389-5)

12. Faruque I, Humbert JS. 2010 Dipteran insect flight dynamics. Part 1 Longitudinal motion about hover. *J. Theor. Biol.* **264**, 538–552. (doi:10.1016/j.jtbi.2010.02.018)

13. Ristroph L, Ristroph G, Morozova S, Bergou AJ, Chang S, Guckenheimer J, Wang ZJ, Cohen I. 2013 Active and passive stabilization of body pitch in insect flight. *J. R. Soc. Interface* **10**, 20130237. (doi:10.1098/rsif.2013.0237)

14. Gao N, Aono H, Liu H. 2011 Perturbation analysis of 6DoF flight dynamics and passive dynamic stability of hovering fruit fly *Drosophila melanogaster*. *J. Theor. Biol.* **270**, 98–111. (doi:10.1016/j.jtbi.2010.11.022)

15. Liang B, Sun M. 2013 Nonlinear flight dynamics and stability of hovering model insects. *J. R. Soc. Interface* **10**, 20130269. (doi:10.1098/rsif.2013.0269)

16. Xu N, Sun M. 2013 Lateral dynamic flight stability of a model bumblebee in hovering and forward flight. *J. Theor. Biol.* **319**, 102–115. (doi:10.1016/j.jtbi.2012.11.033)

17. Zhang Y, Sun M. 2010 Dynamic flight stability of a hovering model insect: lateral motion. *Acta Mech. Sin.* **26**, 175–190. (doi:10.1007/s10409-009-0303-1)

18. Sun M. 2014 Insect flight dynamics: stability and control. *Rev. Mod. Phys.* **86**, 615–646. (doi:10.1103/RevModPhys.86.615)

19. Pérez-Arancibia NO, Ma KY, Galloway KC, Greenberg JD, Wood JR. 2011 First controlled vertical flight of a biologically inspired microrobot. *Bioinspir. Biomim.* **6**, 036009. (doi:10.1088/1748-3182/6/3/036009)

20. Nalbach G. 1994 Extremely non-orthogonal axes in a sense organ for rotation: behavioural analysis of the dipteran haltere system. *Neuroscience* **61**, 149–163. (doi:10.1016/0306-4522(94)90068-X)

21. Dickinson MH. 1999 Haltere-mediated equilibrium reflexes of the fruit fly, *Drosophila melanogaster*. *Phil. Trans. R. Soc. Lond. B* **354**, 903–916. (doi:10.1098/rstb.1999.0442)

22. Sherman A, Dickinson MH. 2004 Summation of visual and mechanosensory feedback in *Drosophila* flight control. *J. Exp. Biol.* **207**, 133–142. (doi:10.1242/jeb.00731)

23. Sherman A, Dickinson MH. 2003 A comparison of visual and haltere-mediated equilibrium reflexes in the fruit fly *Drosophila melanogaster*. *J. Exp. Biol.* **206**, 295–302. (doi:10.1242/jeb.00075)

24. Sugiura H, Dickinson MH. 2009 The generation of forces and moments during visual-evoked steering maneuvers in flying *Drosophila*. *PLoS ONE* **4**, e4883. (doi:10.1371/journal.pone.0004883)

25. Hengstenberg R, Sandeman D, Hengstenberg B. 1986 Compensatory head roll in the blowfly *Calliphora* during flight. *Proc. R. Soc. Lond. B* **227**, 455–482. (doi:10.1098/rspb.1986.0034)

26. Srinivasan MV. 1977 A visually-evoked roll response in the housefly. *J. Comp. Physiol.* **119**, 1–14. (doi:10.1007/BF00655868)

27. Waldmann B, Zarnack W. 1988 Forewing movements and motor activity during roll manoeuvers in flying desert locusts. *Biol. Cybern.* **59**, 325–335. (doi:10.1007/BF00332923)

28. Lehmann F-O and Dickinson M.H. 1998 The control of wing kinematics and flight forces in fruit flies (*Drosophila* spp). *J. Exp. Biol.* **201**, 385–401.

29. Zanker J. 1990 The wing beat of *Drosophila melanogaster*. III. Control. *Phil. Trans. R. Soc. Lond. B* **327**, 45–64. (doi:10.1098/rstb.1990.0042)

30. Windsor SP, Bomphrey RJ, Taylor GK. 2014 Vision-based flight control in the hawkmoth *Hyles lineata*. *J. R. Soc. Interface* **11**, 20130921. (doi:10.1098/rsif.2013.0921)

31. Fry SN, Sayaman R, Dickinson MH. 2005 The aerodynamics of hovering flight in *Drosophila*. *J. Exp. Biol.* **208**, 2303–2318. (doi:10.1242/jeb.01612)

32. Bender JA, Dickinson MH. 2006 Visual stimulation of saccades in magnetically tethered *Drosophila*. *J. Exp. Biol.* **209**, 3170–3182. (doi:10.1242/jeb.02369)

33. Hengstenberg R. 1988 Mechanosensory control of compensatory head roll during flight in the blowfly *Calliphora erythrocephala* Meig. *J. Comp. Physiol. A* **163**, 151–165. (doi:10.1007/BF00612425)

34. Hensler K, Robert D. 1990 Compensatory head rolling during corrective flight steering in locusts. *J. Comp. Physiol. A* **166**, 685–693. (doi:10.1007/BF00240018)

35. Schilstra C, Van Hateren J. 1998 Stabilizing gaze in flying blowflies. *Nature* **395**, 654. (doi:10.1038/27114)

36. Hateren J, Schilstra C. 1999 Blowfly flight and optic flow. II. Head movements during flight. *J. Exp. Biol.* **202**, 1491–1500.

37. Boeddeker N, Hemmi JM. 2010 Visual gaze control during peering flight manoeuvres in honeybees. *Proc. R. Soc. B* **277**, 1209–1217. (doi:10.1098/rspb.2009.1928)

38. Viollet S, Zeil J. 2013 Feed-forward and visual feedback control of head roll orientation in wasps (*Polistes humilis*, Vespidae, Hymenoptera). *J. Exp. Biol.* **216**, 1280–1291. (doi:10.1242/jeb.074773)

39. Ristroph L, Bergou AJ, Ristroph G, Coumes K, Berman GJ, Guckenheimer J, Wang ZJ, Cohen I. 2010 Discovering the flight autostabilizer of fruit flies by inducing aerial stumbles. *Proc. Natl Acad. Sci. USA* **107**, 4820–4824. (doi:10.1073/pnas.1000615107)

40. Tanaka K, Kawachi K. 2006 Response characteristics of visual altitude control system in *Bombus terrestris*. *J. Exp. Biol.* **209**, 4533–4545. (doi:10.1242/jeb.02552)

41. Graetzel CF, Nelson BJ, Fry SN. 2010 Frequency response of lift control in *Drosophila*. *J. R. Soc. Interface* **7**, 1603–1616. (doi:10.1098/rsif.2010.0040)

42. Hyslop A, Krapp HG, Humbert JS. 2010 Control theoretic interpretation of directional motion preferences in optic flow processing interneurons. *Biol. Cybern.* **103**, 353–364. (doi:10.1007/s00422-010-0404-8)

43. Rohrseitz N, Fry SN. 2011 Behavioural system identification of visual flight speed control in *Drosophila melanogaster*. *J. R. Soc. Interface* **8**, 171–185. (doi:10.1098/rsif.2010.0225)

44. Cheng B, Deng X, Hedrick TL. 2011 The mechanics and control of pitching manoeuvres in a freely flying hawkmoth (*Manduca sexta*). *J. Exp. Biol.* **214**, 4092–4106. (doi:10.1242/jeb.062760)

45. Schnell B, Weir PT, Roth E, Fairhall AL, Dickinson MH. 2014 Cellular mechanisms for integral feedback in visually guided behavior. *Proc. Natl Acad. Sci. USA* **111**, 5700–5705. (doi:10.1073/pnas.1400698111)

46. Ristroph L, Berman GJ, Bergou AJ, Wang ZJ, Cohen I. 2009 Automated hull reconstruction motion tracking (HRMT) applied to sideways maneuvers of free-flying insects. *J. Exp. Biol.* **212**, 1324–1335. (doi:10.1242/jeb.025502)

47. Eaton RC. 1984 *Neural mechanisms of startle behavior*. Berlin, Germany: Springer.

48. Cheng B, Fry SN, Huang Q, Dickson WB, Dickinson MH, Deng X. 2009 Turning dynamics and passive damping in flapping flight. In *IEEE Int. Conf. on Robotics and Automation*, pp. 1889–1896. (doi:10.1109/ROBOT.2009.5152826)

49. Bertholf LM. 1932 The extent of the spectrum of Drosophila and the distribution of stimulative efficiencey in it. *Zeitschrift für vergleichende Physiologie* **18**, 32–64.

50. Young J, Walker SM, Bomphrey RJ, Taylor GK, Thomas AL. 2009 Details of insect wing design and deformation enhance aerodynamic function and flight efficiency. *Science* **325**, 1549–1552. (doi:10.1126/science.1175928)

51. Dickinson MH, Lehmann FO, Sane SP. 1999 Wing rotation and the aerodynamic basis of insect flight. *Science* **284**, 1954–1960. (doi:10.1126/science.284.5422.1954)

52. Goodman LJ. 1960 The landing responses of insects. I. The landing response of the fly, *Lucilia sericata*, and other Calliphorinae. *J. Exp. Biol.* **37**, 854–878.

53. Borst A. 1986 Time course of the houseflies' landing response. *Biol. Cybern.* **54**, 379–383. (doi:10.1007/BF00355543)

54. Van Breugel F, Dickinson MH. 2012 The visual control of landing and obstacle avoidance in the fruit fly *Drosophila melanogaster*. *J. Exp. Biol.* **215**, 1783–1798. (doi:10.1242/jeb.066498)

55. Ma KY, Chirarattananon P, Fuller SB, Wood RJ. 2013 Controlled flight of a biologically inspired, insect-scale robot. *Science* **340**, 603–607. (doi:10.1126/science.1231806)

56. Sane SP, Dickinson MH. 2002 The aerodynamic effects of wing rotation and a revised quasi-steady model of flapping flight. *J. Exp. Biol.* **205**, 1087–1096.

57. Berman GJ, Wang JZ. 2007 Energy-minimizing kinematics in hovering insect flight. *J. Fluid Mech.* **582**, 153–167. (doi:10.1017/S0022112007006209)

58. Pringle J. 1948 The gyroscopic mechanism of the halteres of diptera. *Phil Trans. R. Soc. Lond. B* **233**, 347–384. (doi:10.1098/rstb.1948.0007)

59. Nalbach G. 1993 The halteres of the blowfly *Calliphora*. *J. Comp. Physiol. A* **173**, 293–300. (doi:10.1007/BF00212693)

60. Weis-Fogh T. 1973 Quick estimates of flight fitness in hovering animals, including novel mechanisms for lift production. *J. Exp. Biol.* **59**, 169–230.

61. Fotowat H, Fayyazuddin A, Bellen HJ, Gabbiani F. 2009 A novel neuronal pathway for visually guided escape in *Drosophila melanogaster*. *J. Neurophysiol.* **102**, 875–885. (doi:10.1152/jn.00073.2009)

62. Eaton RC, Bombardieri RA, Meyer DL. 1977 The Mauthner-initiated startle response in teleost fish. *J. Exp. Biol.* **66**, 65–81.

63. Gronenberg W. 1995 The fast mandible strike in the trap-jaw ant *Odontomachus*. 1. Temporal properties and morphological characteristics. *J. Comp. Physiol. A* **176**, 391–398. (doi:10.1007/BF00219064)

64. Camhi JM, Nolen TG. 1981 Properties of the escape system of cockroaches during walking. *J. Comp. Physiol.* **142**, 339–346. (doi:10.1007/BF00605446)

65. Jindrich DL, Full RJ. 2002 Dynamic stabilization of rapid hexapedal locomotion. *J. Exp. Biol.* **205**, 2803–2823.

66. Hedrick TL, Cheng B, Deng X. 2009 Wingbeat time and the scaling of passive rotational damping in flapping flight. *Science* **324**, 252–255. (doi:10.1126/science.1168431)

Supplementary Information

(Dated: January 15, 2015)

I. MOVIES

Movie 1:- A fruit fly undergoing a typical roll perturbation and correction maneuver, corresponding to the same data shown in Figure 2. The three sides of of the 3D box show the raw movies from the three fast cameras. The 3D-rendered fly represents the kinematic data of the body and wing positions in each frame. The fly's center-of-mass trajectory is shown by a green line, on which the red segment corresponds to the location of the perturbation. The time in ms is shown on the bottom left corner. The movie is played three times to show the same maneuver from different views. The third time also shows traces of the wing-tip positions.

Movie 2:- Roll perturbation and correction maneuver during nearly-hovering flight. The fly was perturbed $35°$ to its right and corrected to 10% of the perturbation within $T_c = 25$ms, or 5.5 wing-beats. Full correction $\rho = 0$ was obtained at $t = 28$ms. By 40ms the fly shows a slight over-correction to $\rho = -5°$. The yaw deflection that accompanied the roll perturbation is also seen.

Movie 3:- Roll perturbation and correction maneuver in which the perturbation was applied when the fly was already rolled by $20°$ to the right. Prior to the perturbation the fly was also flying with apparent side-slip. The fly corrected to zero roll 30ms after the onset of the perturbation. A yaw-right deflection as a result of the external torque is evident.

Movie 4:- Roll correction maneuver following two consecutive perturbation pulses. When the movie starts the fly is already correcting for the first pulse. The second pulse is applied at $t = 0$ for 5ms. The leg-spreading response as a result of the first pulse is clearly seen. This correction maneuver is indistinguishable from maneuvers following single-perturbation pulses, in terms of the body and wing kinematics as well as the parameters of the PI controller. The corresponding data is shown in Figures S2 and S3.

Movie 5:- Extreme roll perturbation event, corresponding to Fig. 7. The fly was rolled 8 full times to its right by a series of magnetic pulses. The fly regained control $3 - 4$ wing-beats after the perturbation ended. Full correction to $\rho = 0$ was not captured in the movie since the fly exited the filming volume. Note that during the perturbation the fly was unable to oppose the magnetic torque. In fact, the right wing, which in a typical correction maneuver should have been flapping with a larger stroke amplitude, hardly flapped at all and occasionally even seemed disconnected from its flight power muscles.
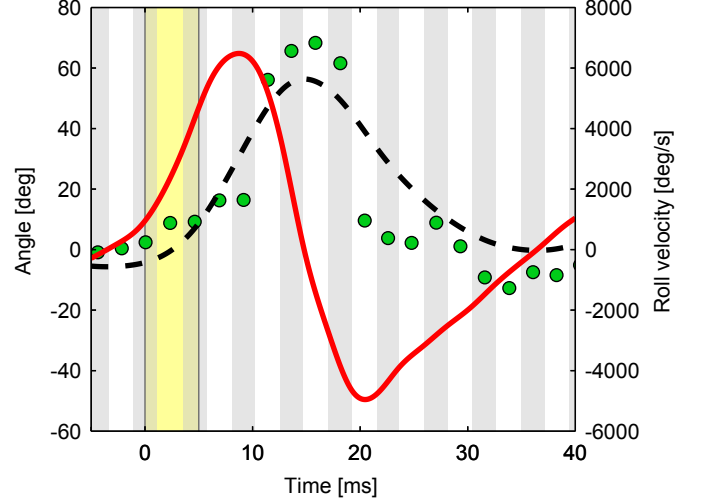

FIG. S.1. The roll angle (black dashed line), roll velocity (solid red line) and the fly's response $\Delta\Phi$ (green circles) as a function of time, for the correction maneuver in Figures 1 and 2 in the main text. The vertical gray stripes indicate back strokes and the white stripes indicate forward strokes. Note the two vertical axis measuring angle (for ρ and $\Delta\Phi$) and angular velocity (for $\dot\rho$).

II. ROLL AND $\Delta\Phi$ KINEMATICS

Figure S.1 shows the roll angle (dashed), roll velocity (red) and the fly's response $\Delta\Phi$ (green circles) as a function of time, for the correction maneuver in Figures 1 and 2 in the main text. The fly's response is almost instantaneous with the roll kinematics, supporting our result that an I-only control model, in which $\Delta\Phi \propto \rho$, must have an unfeasibly small response time. The roll velocity rises and peaks before the roll angle, thus a PI control model that includes the roll velocity follow the changes in the roll angle despite its latency.

III. CONTROL MODEL FITTING

To fit the parameters of the PI control model $\Delta\Phi_{\text{model}}$ (Eq. 3) to the measured data we define the following error function:

$$E(\Delta T, K_{\mathrm{p}}, K_{\mathrm{i}}) = \frac{1}{N} \sum_{j=1}^{N} \left[\Delta\Phi_{\mathrm{model}}(\Delta T, K_{\mathrm{p}}, K_{\mathrm{i}}, t_j) - \right.$$

$$\left. \Delta\Phi_{\mathrm{expr}}(t_j) \right]^2, \qquad (\text{S.1})$$

whose minimization gives the three fitted parameters. The discrete times t_j are the mid-halfstroke times when $\Delta\Phi_{\mathrm{expr}}(t_j)$ was measured (green circles in Figs. 2, S.4f). The fit process considered data measured between $t = \Delta T$ and $t = 40\mathrm{ms}$, to include only the correction maneuver. Because $E(\Delta T, K_{\mathrm{p}}, K_{\mathrm{i}})$ is fast to calculate and the range of each of its parameter could be readily confined, we were able to evaluate the error function on a grid in the 3D parameter space and directly examine the structure of the error function. We could limit the range of each parameter, for example, ΔT is positive and bounded by the duration of the entire correction maneuver. The other two parameters are either zero or positive and their upper search bounds were determined based on reasonable cut offs given the trends in the errors. Hence, we could directly verify that the function has a single global minimum within the evaluated parameter range. The minimum was obtained on one of the grid points. The grid spacing was fine enough such that going to nearby points had negligible change in the cost function compared with measurement accuracy. Fig. S.2 illustrates the error landscape for the maneuver shown in Fig. 2, by plotting the contours of $E - E_{\mathrm{min}}$ in three orthogonal cross sections around the global minimum E_{min}.

We use such plots to evaluate the confidence intervals (CI) of the fitted controller parameters. We assume that the distribution of the measurement error of $\Delta\Phi_{\mathrm{expr}}$ is Gaussian, $N(0, \sigma^2)$, with zero mean and $\sigma = 2°$. This measurement error was evaluated in a previous paper by our group [1] and also verified manually for each wing stroke in the current data set. The reduced error function is, therefore, $e = E/\sigma^2$. If the model perfectly predicted the data, the reduced error function becomes a sum of the squares of N independent standard normal random variables, namely, the χ^2 distribution. The confidence interval is obtained by evaluating the change in a parameter that results in a unity change in e or, equivalently, a σ^2 change in the error function E. In Fig. S.2 the contour of $\sigma^2 = 4$ corresponds to the estimated confidence intervals of the three fitted parameters in the specific maneuver: $\Delta T = 4.4 \pm 0.25\mathrm{ms}$, $K_{\mathrm{p}} = 6 \pm 0.5\mathrm{ms}$, and $K_{\mathrm{i}} = 0.7 \pm 0.05$.

IV. RECOVERY FROM A DOUBLE PULSE PERTURBATION

Figures S.3 and S.4 show measured data for a recovery maneuver from a double pulse perturbation (Movie 4). The results show the same correction mechanism as for a single pulse perturbation (Figures 1 and 2 in the main text).

V. ANALYZING PREVIOUSLY PUBLISHED DATA ON ROLL RESPONSE OF TETHERED FLIES

To further test the PI control model, we used it to predict the roll-response of tethered fruit flies previously published by Dickinson in [2]. In these tethered experiments flies were mounted on a gimbaled apparatus oscillating along a given axis, such that the flies had no visual cues relating to the imposed rotation. The wing-stroke amplitudes were measured using phorodetectors that recorded the shadow of each wing. We focus on the roll-response measurements, in which flies were oscillated along a horizontal roll axis termed "functional roll" (h_{b} in Fig. 1c in the main text). Although this axis is different than the Euler roll axis considered in this paper, it can be shown for a fly pitched up by 45°, a given rotation along the "functional roll" generates almost the same deflection along the Euler roll. Hence, when discussing rotations along the Euler roll angle, the two roll definitions are practically equivalent.

The stroke amplitude of the left wing was measured during an oscillating roll perturbation with an amplitude $A = 25°$, period $T = 0.63\mathrm{s}$, and a maximum roll velocity of $250°\mathrm{s}^{-1}$. The roll angle is described by $\rho(t) = A\sin(\omega t)$ and the roll velocity is $\dot{\rho}(t) = A\omega\cos(\omega t)$. The wing response data was plotted both as a function of the roll angle (Fig. 3d, [2]) and roll velocity (Fig. 3e, [2]). We applied standard image analysis techniques to extract the data from these two plots and used the data to find the parameters of the corresponding PI controller, as described below (Figs. S.5 and S.6).

Since the roll oscillation period in the tethered experiment is 630ms, the time delay measured in the free flight experiments $\Delta T \approx 5\mathrm{ms}$ is negligible. Hence the response in the tethered experiment is effectively instantaneous and the functional form of the controller can be written as:

$$\Delta\Phi_{\mathrm{Left}}(t) = \frac{1}{2}\left(K_{\mathrm{p}}\dot{\rho}(t) + K_{\mathrm{i}}\rho(t) \right), \qquad (\text{S.2})$$

in which $\Delta\Phi_{\mathrm{Left}}(t) \equiv \Phi_{\mathrm{Left}}(t) - \Phi_{\mathrm{Mean}}$ is the deviation of the left wing amplitude from its mean value Φ_{Mean}. The $\frac{1}{2}$ factor is due to the fact that data was measured for the left wing rather than for the stroke amplitude difference between the wings (as in Eq. 3 in the main text). Twice the slope of the linear fit to $\Phi_{\mathrm{Left}}(\dot{\rho})$ reported in [2] was used to obtain $K_{\mathrm{p}} = 32.2\mathrm{ms}$. To obtain K_{i} we manually fit the data and obtain a value of $K_{\mathrm{i}} = 0.2$. A fitting algorithm was not used for K_{i}, because many data points were clustered near $\pm 25°$ and could not be extracted.

The prediction of the PI controller fit are plotted in Figs. S.5 and S.6 along with the extracted data from [2]. Fig. S.5a shows that the prediction of the PI model plotted as a function of the roll angle yields an ellipse with $R^2 = 0.77$. Similarly, the PI model prediction as a function of the roll velocity (Fig. S.5b) also yields an ellipse
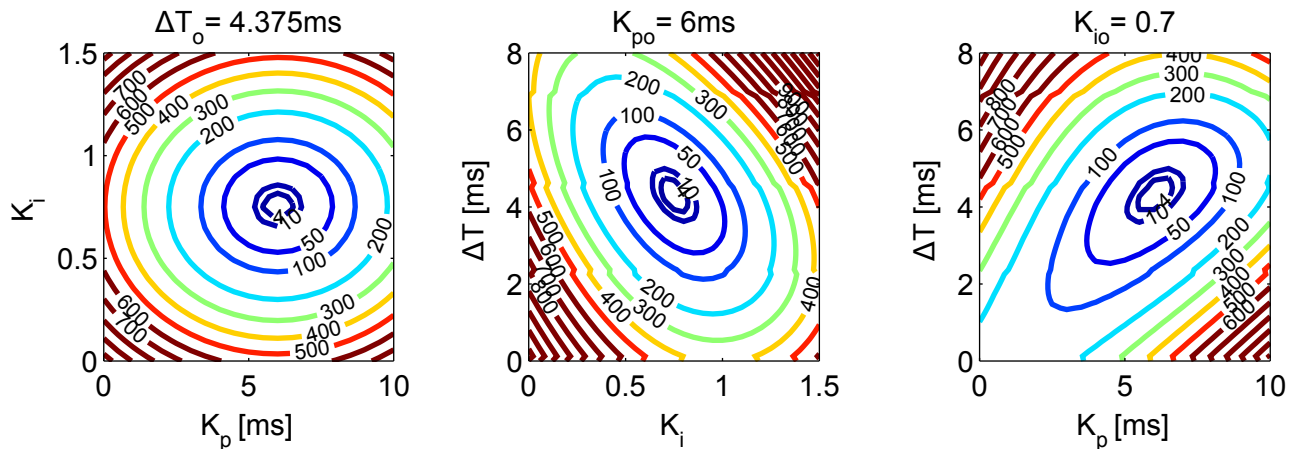
FIG. S.2. The error landscape for the fitting process of a PI controller model for the movie shown in Figs. 1 and 2 of the main text. The three panels show contours of the error function $E(\Delta T, K_{\mathrm{p}}, K_{\mathrm{i}})$ in three orthogonal cross section that coincide at the minimum of E. The numerical values of the minimizing parameters $(\Delta T_{\mathrm{o}}, K_{\mathrm{po}}, K_{\mathrm{io}})$ are given in the title of each panel. The inner-most counter of $\sigma^2 = 4$ corresponds to the evaluated confidence interval.

with $R^2 = 0.82$ (compared with $R^2 = 0.62$ of the linear fit). The measured data and PI-model prediction are also plotted in the 3D space whose axes are $(\rho, \dot{\rho}, \Phi_{\mathrm{Left}})$ (Fig. S.6). We find that the Φ_{Left} output as a function of the $(\rho, \dot{\rho})$ stimulus is well described by an inclined ellipse.

The 3D shape of the response Φ_{Left} as a function of $(\rho, \dot{\rho})$ lies on a plane defined by (Eq. S.2). In this particular case, the stimulus is sinusoidal in time so that in the $(\rho, \dot{\rho})$ plane it forms an ellipse. The corresponding response is an inclined ellipse that lies on the response plane. Hence, plotting the projections of the 3D ellipse, as in the plots of $\Phi_{\mathrm{Left}}(\rho)$ and $\Phi_{\mathrm{Left}}(\dot{\rho})$ in [2], each yield an ellipse (Fig.S.5a,b).

Intuitively, the upper right quadrant of the ellipse in Fig.S.5a corresponds to times when the fly is rolled to its left ($\rho > 0$) with a leftward roll velocity ($\dot{\rho} > 0$). The response is maximum at these times because the two terms of the PI controller are positive (Eq. S.2). The bottom right quadrant of the ellipse in Fig.S.5a corresponds to times when the fly is rolled to its left ($\rho > 0$) but with a rightward roll velocity ($\dot{\rho} < 0$). The response at these times is smaller than at the upper left quadrant since the two terms in Eq. S.2 have opposite signs. Similarly, the response is minimum when $\rho < 0$ and $\dot{\rho} < 0$ (bottom left quadrant).

Finally, following [2], we plot the fly's response as a function of the roll acceleration (Fig. S.7), along with the prediction of the PI control model. Note, that the PI model is a function of roll angle and roll velocity, and does not use information about roll acceleration. Still, the plot shows that the PI model can explain the observed behavior without using the roll acceleration. It supports the hypothesis that fruit flies do not measure their roll acceleration.

The prediction of the PI controller model is also consistent with measurement of the temporal response of a fly to a roll perturbation (Fig. 2 in [2]). The tethered

experiment showed a mean stroke amplitude difference between the two wings of $\Delta\Phi = 8°$ (peak-to-peak) in response to an sinusoidal roll stimulus of $25°$ amplitude and 0.8s period. Using the PI controller (Eq. 3 in the main text) with the parameters fitted above predicts a response of $\Delta\Phi = 8.0°$. Moreover, the phase of the response with respect to the stimulus is also predicted by the model. The peak asymmetry was observed at times between the maxima of ρ and the maxima of $\dot{\rho}$, implying that both terms of Eq. S.2 have comparable contributions to the response, as we see in the free flight experiments.

The values of the controller parameters fitted for the tethered experiment are different than the controller parameters fitted to the free flight experiment reported here (Table II). Possible reasons for this difference are natural variablity among flies (as characterized by the free flight data) as well as the different experimental methods: using tethered compared to free flying animals.

In summary, the PI controller well-describes results of previous experiments with tethered flies, with a correlation coefficient between the predicted and measured wing amplitude of 0.91. Moreover, the tethered flies were placed in a sealed apparatus such that they did not have any visual cue about the imposed rotation, suggesting that the fly's roll response is mediated by mechanical sensors, consistent with the PI control model.
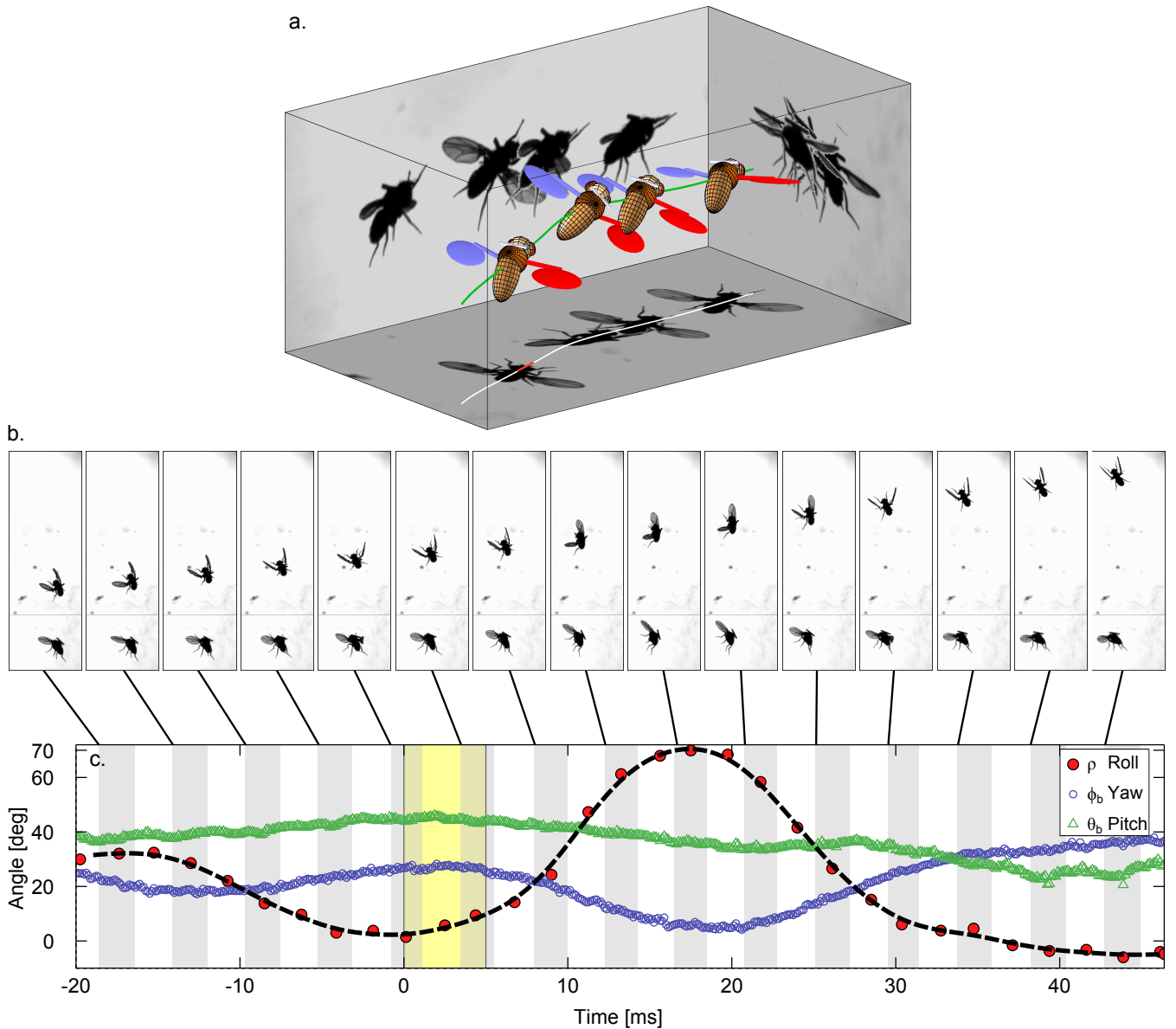
FIG. S.3. Roll perturbation and correction following a double-pulse perturbation. (a) Images from three orthogonal fast cameras of a fruit fly undergoing the perturbation and correction maneuver. Each panel shows 4 superimposed images, before, during and after the second perturbation pulse. The 3D-rendered fly represents the kinematic data of the body and wings. The location of the perturbation (red line) is shown on the fly's center-of-mass trajectory (green line). The second snapshot shows the fly rolled to $70°$ to its right due to the second perturbation pulse. (b) Top and side-view snapshots of 15 consecutive wing-strokes during the maneuver. Snapshots were taken at the same phase along the wing-stroke, where the wings are in their forward-most position. The snapshots show a clear asymmetry in the wing-stroke amplitude, such that the right wing increased its amplitude and the left wing decreased its amplitude. (c) The body Euler angles during the maneuver. The first perturbation torque was not captured in the movie, but the perturbation of $37°$ in roll and the recovery are seen in $t = (-20) - 0$ms. The second perturbation torque was on between $0 - 5$ms (yellow stripe), and resulted in a $70°$ rightward roll deflection. The white and gray stripes represent forward- and back-strokes, respectively. Yaw and pitch angles were sampled at 8000Hz. The roll angle was measured manually in the middle of every half-stroke and smoothed by a quintic spline (black dashed line). Measurement errors are comparable to the size of the plotted symbols.

VI. ADDITIONAL PI CONTROLLER FITS

Figures S.8 - S.10 show three more examples for the fit of the PI controller model. In addition to the fitted curves (red) these plots show that the response of the fly in terms of its wing stroke amplitude asymmetry is continuous, thereby excluding discontinuous control models.
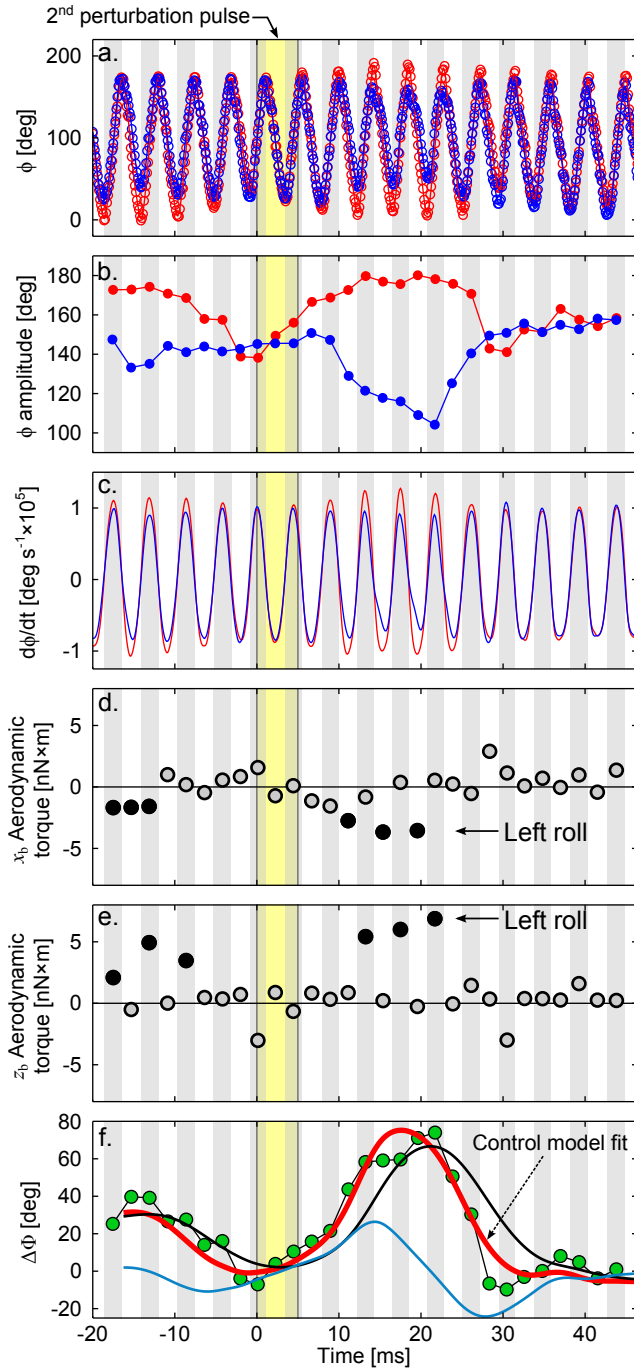
FIG. S.4. Roll correction mechanism for the double-perturbation movie shown in Fig. S1 and Movie 3. (a-c) Wing stroke kinematics as a function of time: (a) The stroke angle ϕ of the right (red) and left (blue) wings; (b) their peak-to-peak amplitude Φ, and (c) their angular velocity $\dot{\phi}$ (c). (d-e) Mean aerodynamic torque along each half stroke, calculated from the measured wing kinematics using a quasi-steady state aerodynamic force model. Solid symbols highlight the correcting wing strokes. (d) the torque component along the body axis $\hat{\mathbf{x}}_b$, such that negative torque induces a corrective left roll; (e) The torque component along $\hat{\mathbf{z}}_b$, such that positive values have corrective effect. (f) Wing stroke amplitude difference $\Delta\Phi$ (green), and a fit for a PI controller (eq. 1, red), with $\Delta T = 3.75$ms, $K_p = 3.5$ms, and $K_i = 0.95$. The contributions of the 1st and 2nd terms of Eq. 1 are shown in blue and black, respectively. Measurement errors in (a-f) are comparable to the symbols size.
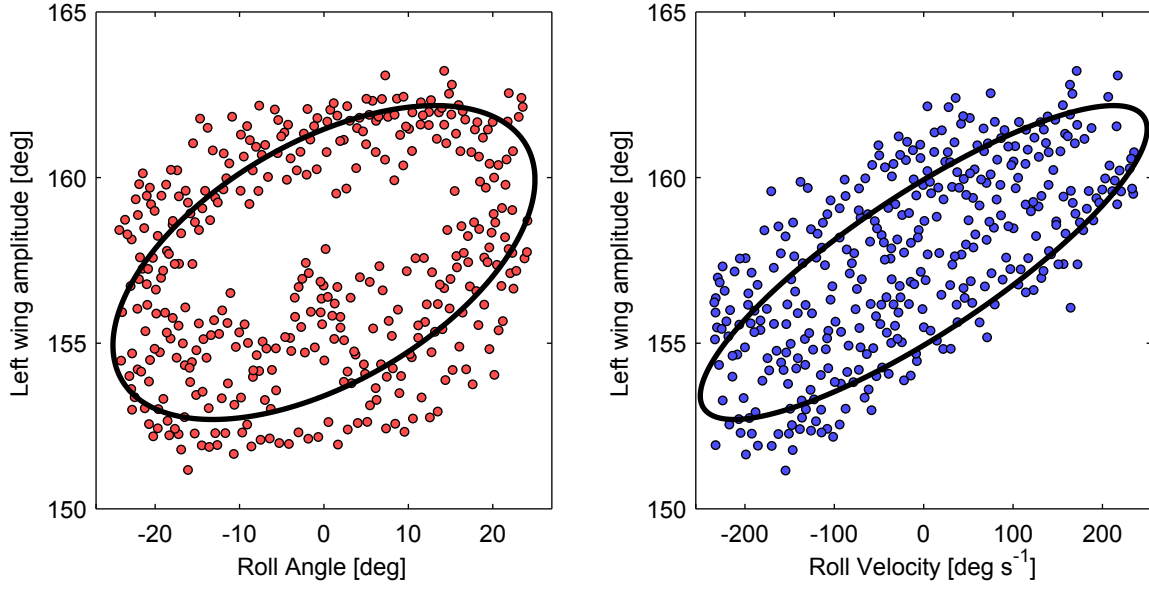
FIG. S.5. The data extracted from [2] for the left wing amplitude in response to a periodic roll oscillation. On the left panel the red circles represent the response to the roll angle. On the right panel the blue circles represent the response to the roll velocity in the same measurement. The black solid ellipses on both panel show the predicted response of a PI control model.
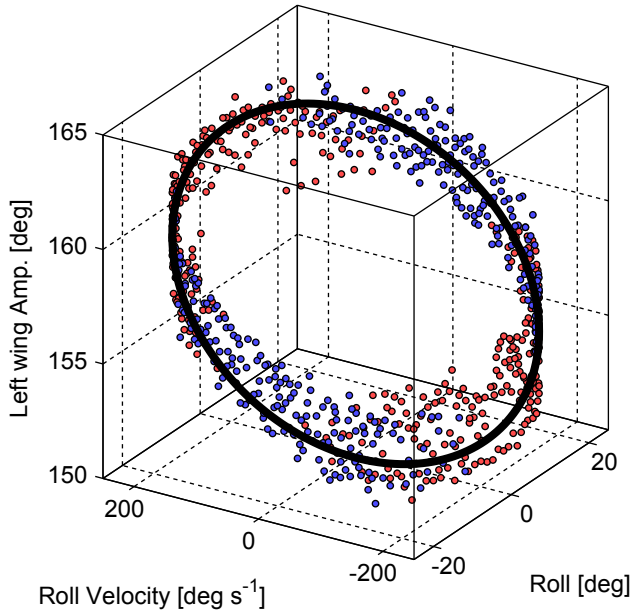

FIG. S.6. The data extracted from [2] for the left wing amplitude in response to a periodic roll oscillation is plotted in the 3D space whose axes are $(\rho, \dot{\rho}, \Phi_{\text{Left}})$. The data points are colored according to their original color in (Fig. S.5). The black solid line shows the predicted response of the same PI control model shown in Fig. S.5.
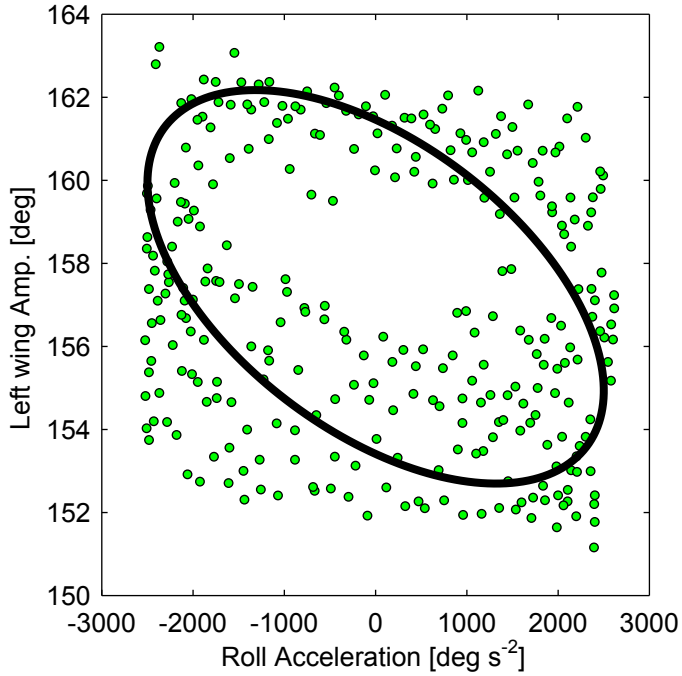
FIG. S.7. The data extracted from [2] for the left wing amplitude in response to a periodic roll oscillation is plotted as a function of roll acceleration. The black solid line shows the predicted response of the same PI control model. Importantly, the PI model is a function of roll angle and roll velocity, and does not include the roll acceleration. The plot shows that the PI model can explain the observed behavior without using the roll acceleration. It supports the hypothesis that fruit flies do not measure their roll acceleration.

[1] L. Ristroph, G. J. Berman, A. J. Bergou, Z. J. Wang, and I. Cohen, Journal of Experimental Biology **212**, 1324 (2009).

[2] M. H. Dickinson, Philosophical Transactions of the Royal Society of London.Series B: Biological Sciences **354**, 903 (1999).

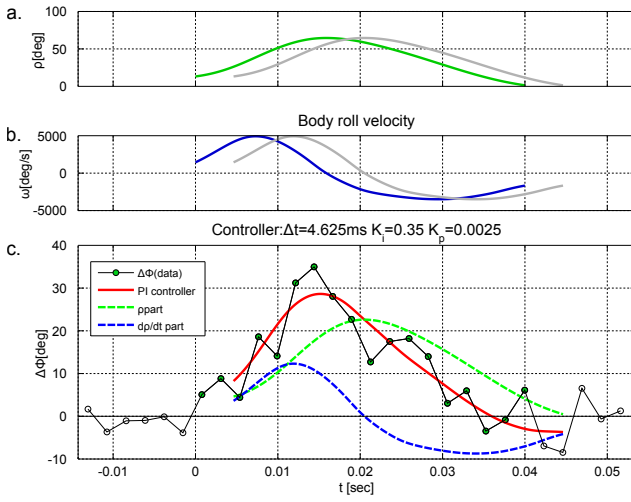FIG. S.8. PI controller fit. (a) The roll angle ρ as a function of time (green). The gray line is ρ shifted by ΔT, which is the fitted time delay for the PI controller model. (b) The roll velocity $\dot{\rho}$ (blue). The gray line is $\dot{\rho}$ shifted by ΔT. (c) The wing stroke amplitude asymmetry (green circles) $\Delta\Phi$ measured as a function of time for each half stroke. The red line is the response of the fitted PI controller. The dashed green line shows the contribution of the integral term of the controller, namely $K_i \rho(t - \Delta T)$. The dashed green line shows the contribution of the proportional term $K_p \dot{\rho}(t - \Delta T)$. Both terms have comparable contrubitions to the overall response.
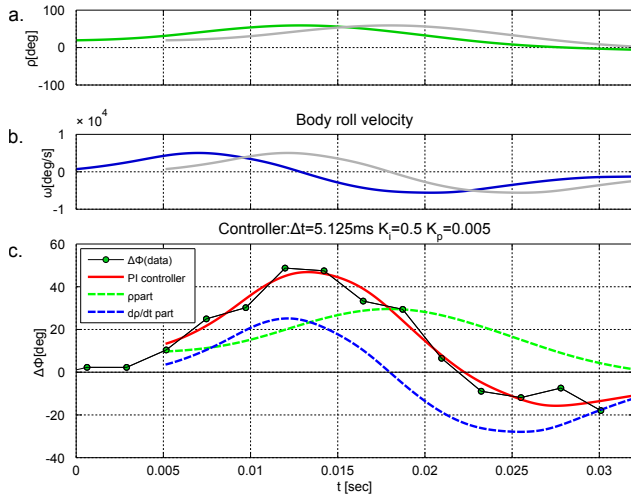

FIG. S.9. Similar plots to the ones in Fig. S.8 for a different correction maneuver.
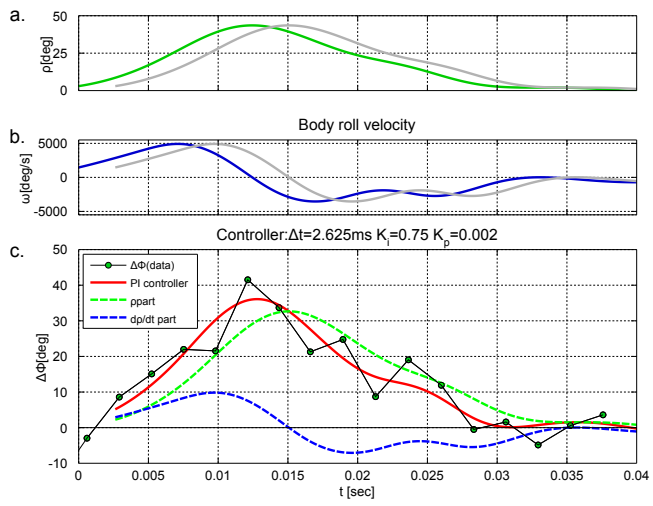
FIG. S.10. Similar plots to the ones in Figs. S.8 and S.9 for a third correction maneuver.